CHARLES UNIVERSITY

Faculty of Science
Department of biochemistry

Study programme: Biochemistry
Branch of study: Biochemistry

Bc. Kryštof Knapp

Structural and functional studies of signaling molecules in axon guidance

Strukturní a funkční studie signalizačních molekul ve vedení axonu

Diploma thesis

Supervisor: Mgr. Daniel Rozbeský, Ph.D.

Prague, 2022

Declaration:

I declare that the work presented here is my own and that all sources of previous knowledge are cited properly. No part of this work was used and will not be used to obtain any other academic degree.

Prague May 18, 2022 ....

Abstrakt:

V této práci jsme se zaměřili na studium autoinhibičního mechanismu proteinů z rodiny MICAL pomocí biochemických, biofyzikálních a bioinformatických metod. MICAL proteiny patří do skupiny flavinových monooxygenas a sehrávají nezbytnou roli v řadě buněčných procesů zejména skrze regulaci dynamiky cytoskeletonu. MICAL-1 je dlouhodobě studován pro svou roli v mechanismu navádění axonu jako efektor repulzivně signalizačních drah, kde působí destabilizaci aktinových vláken pomocí své oxidační aktivity. Nedávno zveřejněné studie poukazují na to, že MICAL-1 může působit také jako signalizační molekula skrze lokalizovanou produkci peroxidu vodíku, která reguluje funkci dalších proteinů. Navzdory tomu, že je dlouhodobě zřejmé, že aktivita MICAL-1 proteinu musí být přísně regulována, přesný mechanismus této regulace dosud není znám. Na základě studia reakční kinetiky a simulací molekulové dynamiky MICAL-1 proteinu z křepelky japonské a jeho zkrácené verze bez C-terminální domény, předkládáme nový model pro autoinhibiční mechanismus MICAL-1 proteinů. Domníváme se, že regulace aktivity MICAL-1 proteinů je zprostředkována skrze interakci mezi C-terminální a monooxygenasovou doménou, která brání plné katalytické aktivitě. Dále předkládáme důkazy o tom, že regulace aktivity proteinu není ovlivněna změnou jeho oligomerního stavu. Výsledky této práce poslouží jako základ pro navazující detailní studii mezidoménových interakcí v MICAL-1 proteinu.

[V angličtině]

Klíčová slova: MICAL-1, Navádění axonu, Plexin, F-aktin, Autoinhibice, Cytoskeleton

Abstract:

This work aims to determine a model of the autoinhibition mechanism of MICAL proteins using biochemical, biophysical, and bioinformatical approaches. MICAL proteins are a group of flavin monooxygenases that play a key role in various cellular processes, as they facilitate the reorganization of the actin cytoskeleton. MICAL-1 has long been known for its vital role in axon guidance as an effector of repulsive signaling through oxidative destabilization of actin filaments. However, recent findings indicate that MICAL-1 can also serve as a signaling molecule, using localized hydrogen peroxide production to regulate other downstream effectors. Despite the consensus that MICAL-1 activity must be strictly regulated, the exact molecular mechanism of this regulation has not yet been described. In this work, we provide a novel model of MICAL-1 autoinibiton mechanism based on a comparison of steady-state kinetic experiments and molecular dynamics simulations between full-length MICAL-1 from *Coturnix japonica* and its truncated form lacking the C-terminal domain. In our model, we conclude that changes in MICAL-1 activity are the result of intramolecular protein interactions between the C-terminal and the monooxygenase domain. Furthermore, we rule out the role of MICAL-1 oligomerization in its activity regulation. Our work provides the basis for further research that will need to focus on a more detailed investigation of intramolecular interactions between the MICAL-1 domains.

Key words: MICAL-1, F-actin, Axon guidance, Plexin, Autoinhibition, Cytoskeleton

Acknowledgement:

I would like to express my gratitude to all those who helped me in my master's studies, especially my supervisor Daniel Rozbeský for the patience and care he treated me with throughout the project and for his selfless support and inspiration he gave me for my future path. Furthermore, I would like to thank Adam Schröfel for introducing me to the intriguing world of electron microscopy and also for his work on the project.

Many thanks go to my lab colleagues for their help and advice they gave me during my lab days, especially to Nicola for her support in moments of experimental failures and Dominika for her patience during late-night experiments. Also, my thanks go to Dr. Jiří Pavlíček for setting up the crystallization experiments and his kind approach. In addition, I wish to thank Ján Sabó for his assistence with the actin preparation.

Finally, I would like to thank my friends and family for their support during my studies.

Contents

List of abbreviations

- AEX - Anion exchange chromatography
- ARP - Actin reacting protein
- CH domain - Calponin homology
- CRMP - Colapsin response mediator protein
- CSPG - Chondroitin sulfate proteoglycan
- DCC - Deleted in colorectal carcinoma
- DTT - Dithiothreitol
- EHBP1 - Eps15-homology domain containing protein
- GAP - GTPase activating protein
- GEF - Guanine nucleotide exchange factor
- GPI - glycophosphatidylinositol
- GTBM - Minimal Myosin Va^{GTD} binding motif
- Glu-rich region - Glutamic acid rich region
- HSPG - Heparan sulfate proteoglycan
- IMAC - Ion-metal affinity chromatography
- Ig-CAM - L1 immunoglobulin superfamily cell adhesion molecule
- K_m - Michaelis constant [μM]
- LIMK - LIM domain kinase
- MALS - Multiangle light scattering
- MICAL - Molecule interacting with CasL
- MICAL-L2 - MICAL-like 2 protein
- MO domain - Monooxygenase domain
- NrCAM - Neural cell adhesion molecule
- Nrp - Neuropilin
- PAE - Predicted aligned error [Å]
- PCR - Polymerase chain reaction
- PlexX - invertebrate plexin
- PlexinX - Vertebrate plexin
- Pro-rich motif - Proline-rich motif
- PrxI - Peroxoredoxin I

- RBD - Rho GTPase binding domain of plexin receptors
- RMSD - Root mean square deviation [nm]
- RMSF - Root mean square fluctuation [nm]
- ROCK - Rho kinase
- RPM - Round per minute
- RTK - Receptor tyrosine kinase
- Robo - Roundabout
- SDS-PAGE - Sodium dodecyl sulphate- polyacrylamide gel electrophoresis
- SEC - Size exclusion chromatography
- SH3 - Src homology 3
- Sema-x - Invertebrate semaphorin
- SemaX - Vertebrate semaphorin
- hMICAL - human MICAL-1
- k_{cat} - catalytic constant [s^{-1}]
- pHBH - para-hydroxybenzoate hydroxylase
- pLDDT - Predicted local distance difference test
- qMICAL - MICAL-1 from *Coturnix japonica*

1 Literature review

1.1 Introduction

During neuronal development, maturing neurons create protrusions, neurites, to find their synaptic partners to form a complex neural network. One of the neurites, the axon, follows a different path from the others, embarking on a long journey to find a receiver of the signal. At the tip of the evolving axon, a special structure called a growth cone is created. The growth cone detects extracellular signals, guidance cues, secreted or displayed by other cells, which navigate the axon through the intercellular space. To date, many guidance signals and their receptors have been discovered, including semaphorins and plexins [1].

Semaphorins are a group of secreted or cell surface guidance cues conserved across a wide range of species. They can act as attractive or repulsive signals, depending not only on the type of semaphorin, but also on the type of receptor [2]. The discovery of MICAL proteins and their participation in the semaphorin-plexin signaling pathway was a major step in the study of axon guidance. MICALs have shown a novel mechanism of cytoskeleton remodeling through the oxidation of amino acid residues of F-actin subunits and therefore have revealed the existence of a long-sought direct link between semaphorin signaling and cytoskeleton reorganization [3, 4]. Despite all advances in this field, the system of MICAL regulation and the exact mechanism of interaction with actin filaments remain elusive. Understanding these mechanisms is even more emerging, as MICALs are involved in many other cellular processes and their deregulation or mutations in their genes are associated with various diseases, including breast cancer or epilepsy [5, 6, 7].

Solving the structure of MICALs can help us elucidate these processes and design drugs that effectively manipulate their activity. Furthermore, understanding the complicated machinery of cytoskeleton remodeling might unravel new options for the targeted treatment of cytoskeleton-related diseases and shed more light on the essential cellular processes in which rearrangement of intracellular scaffolding is necessary.

1.2 Axon guidance and growth cone

The functionality of brain circuits depends on the proper wiring of the neural network, where each cell must bind to its correct interaction partner to form a synapse. To create these connections, propagating axons have to overcome distances ranging from micrometers to the macroscopic scale of meters. Along this path, they are navigated by a highly dynamic structure located at the tip of the propagating axon, termed the growth cone. The role of the growth cone is not only to create the driving force for axon propagation, but also to evaluate and translate diverse extracellular signals into directional growth of the axon.

1.2.1 Growth cone structure

The growth cone is formed by a highly complex structure of actin filaments and microtubules (Fig.1.1 B, page 13). The microtubules entering the growth cone from the axonal rod create a stable core of the growth cone, the central domain (C domain, Fig.1.1 B), whose shape may vary from a pointed cylindrical structure observed in rapidly expanding axons to a large oval-shaped shape in a stopped axon (Fig.1.1 C and D, respectively). The peripheral domain of the growth cone (P domain) contains two types of F-actin structures. Long bundles of F-actin form the filopodia, and a highly interconnected F-actin network called lamellipodia (Fig.1.1 A, B). The structure of some filopodia is further reinforced by microtubule filaments that propagate from the C domain further into the protrusions of the growth cone. The last distinguishable domain of the growth cone, the transition zone (T zone), lies in the interface between the peripheral and central domains and is mainly formed by actin arcs. Actin arcs are contractile structures consisting of F-actin filaments and myosin motors (actomyosin) that surround the core bundle of microtubule filaments that forms the C domain [8, 9, 10].

1.2.2 Molecular mechanism of axon outgrowth

The movement of the axon and the formation and collapse of the protrusions are regulated by dynamic changes in the polymerization of the cytoskeleton. The main driving force that pushes the cytoplasmic membrane of filopodia originates from two processes that occur simultaneously, actin treadmilling and actin retrograde flow. Actin treadmilling is a process in which the depolymerized G-actin subunits of the pointed end of the F-actin filament located in the T zone are continuously transported by actin motors to the barbed end of the filament, which lies at the tip of the filopodia. At the barbed end, F-actin repolymerizes and pushes onto the cell membrane through the Brownian ratchet mechanism [8, 11, 12]. Naturally, the membrane pushes onto F-actin with the same force, resulting in a retrograde flow of F-actin filaments, which is a constant movement of filopodial F-actin filaments towards the center of the growth cone. Whether the retrograde flow is driven solely by F-actin polymerization [13, 14] or is partially driven by myosin motor activity [15, 16] remains controversial, as the results of studies differ. A possible explanation for these controversies can be provided through the evaluation of the role of myosin II in the severing of the F-actin-pointed ends (located in the T zone). Myosin motors, rather than pulling directly on the F-actin filament, can play their role in actin disassembly, which is crucial to support the barbed end of the F-actin filament with a sufficiently high concentration of G-actin for fast polymerization of F-actin [11, 17, 18].

As long as the forces are in balance, there is no protrusion. When the growth cone detects attractive signals, F-actin is bound to "clutch" proteins coupled to receptors in

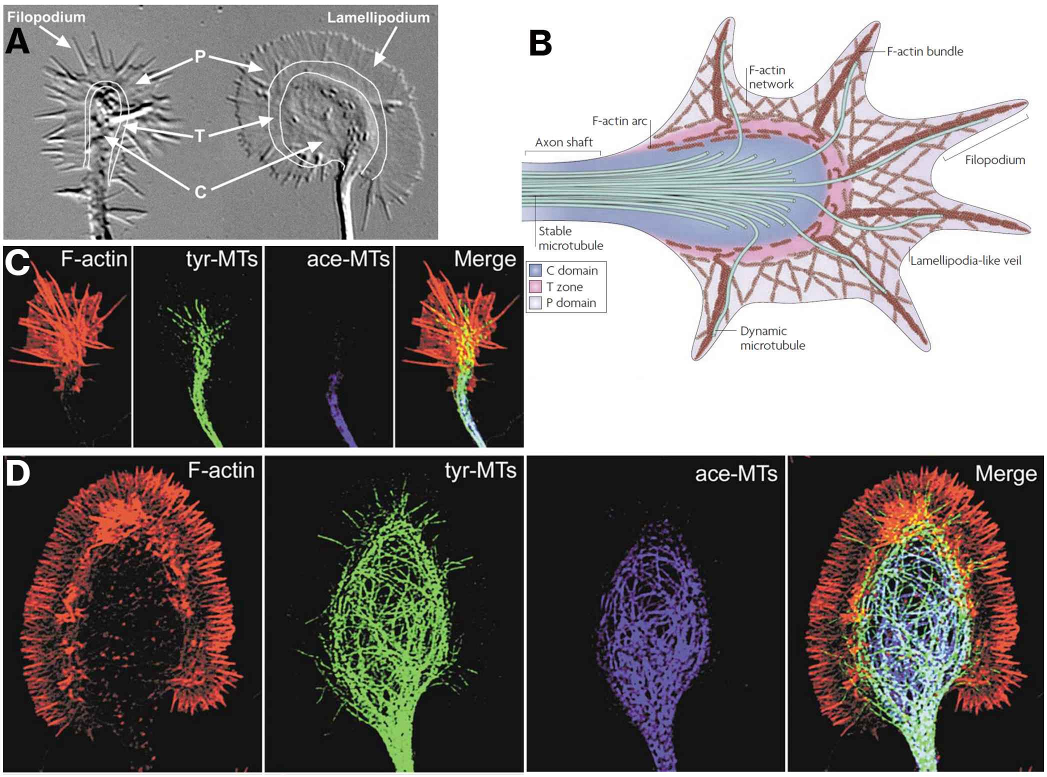

Figure 1.1: ***Structure of the growth cone***
A) Differential interference contrast images of hippocampal growth cones show the diversity of growth cone shapes. B) Schematic drawing of the cytoskeleton organization in the growth cone. The C domain is formed by a large bundle of microtubules entering from the axon shaft. Some microtubules are pioneering into the filopodia and support the F-actin bundles that form the filopodial protrusions. Microtubules in the C domain are consolidated by contractile actomyosin structures, which form the T zone. F-actin bundles and the F-actin network forming the filopodia and lamellipodia, respectively, originate in the T zone. Severing of F-actin, that is necessary for proper F-actin turnover, also occurs in the T zone. Fixed and labeled rapidly elongating hippocampal axon C) and paused hippocampal axon D). Both are shown at the same magnification. F-actin is labeled with phalloidin and microtubules with specific antibodies against tyrosinated (tyr-MTs) and acetylated microtubules (ace-MTs). Tyrosination occurs predominantly on the newly formed microtubule, whereas acetylation correlates directly with the age of the microtubule. Adapted from [9] and [8].

the walls of filopodia. This leads to a stoppage of retrograde flow, and polymerization of F-actin can effectively push the cell membrane and cause its protrusion [8]. In the next stage, the microtubules that form the C domain elongate in the direction of protrusion, moving the C domain forward. The tubulin bundles are then compressed by actin arcs, and the back part of the growth cone is consolidated into the newly formed axon shaft [9].

Regulation of cytoskeleton dynamics by Rho GTPases

Signaling pathways are highly interconnected, which is essential for the ability to precisely translate multiple overlapping chemical gradients of guidance signals into sophisticated responses. To illustrate, binding of netrin to a DCC receptor (Deleted in Colorectal Carcinoma) leads not only to activation of α-chimerin, which belongs to a group of GTPase activating proteins (GAPs), but also to activation of TRIO guanine nucleotide exchange factor (GEF) [8, 19]. Both of these factors further interact with Rho GTPases, generally GEFs activate GDP-bound GTPases by replacing GDP with GTP, while GAPs inactivate by promoting their GTPase activity (fig. 1.2 box, page 15). Among others, TRIO and α-chimerin both interact with RacI Rho GTPase, but each of them interacts in an opposite manner [8]. Whether RacI will be predominantly in an active or inactive state must therefore be dependent on its interaction with other GAPs/GEFs.

Another Rho GTPase, RhoA, is regulated similarly by two GEFs, ephexin and TRIO, and one GAP, p190RhoGAP. However, in this case, the situation is rather different, as regulation factors are influenced by at least four different signaling pathways (Fig. 1.2). Ephexin is a downstream effector in the Ephrin/Eph (ligand/receptor) pathway [20], TRIO is activated by the Netrin/DCC system as already mentioned, as well as by the Slit/Robo pathway. Finally, p190RhoGAP is triggered by the Semaphorin/Plexin signaling [8].

To date, around 80 GAPs, 82 GEFs and 20 Rho GTPases have been discovered in eukaryotes [21]. Although not all are directly involved in the axon guidance, the complexity of the regulation of the navigation system by Rho GTPases is apparent, not to mention their involvement in the regulation of microtubules [22].

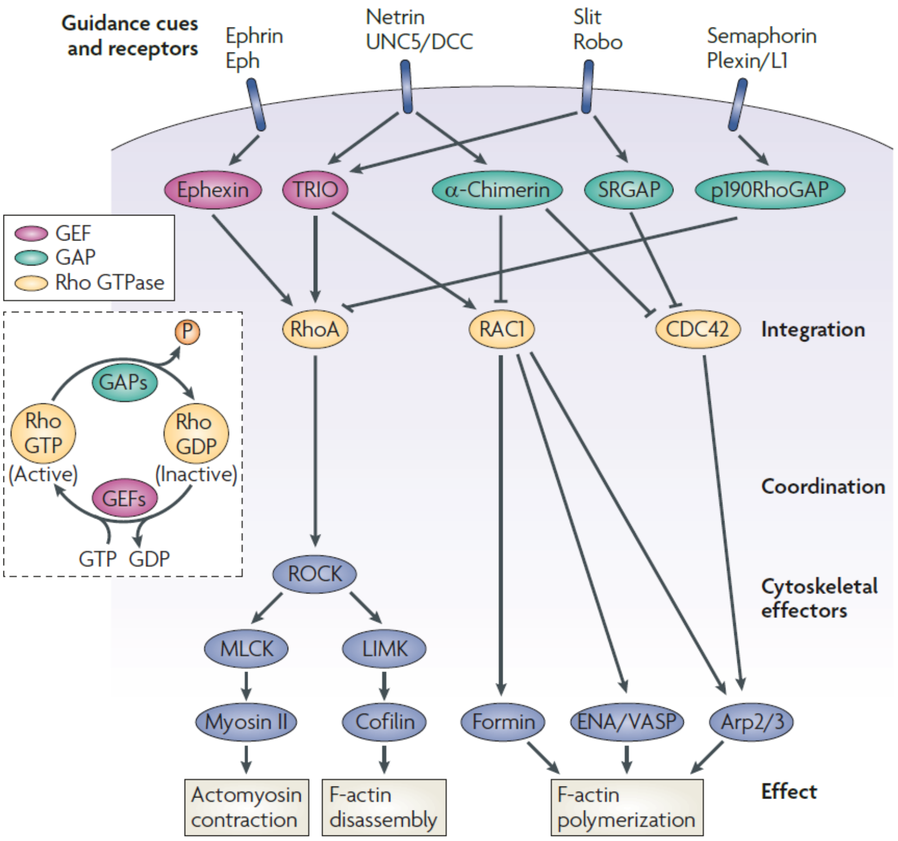

Figure 1.2: ***Rho GTPases signaling pathways in axon guidance***
Axon guidance is controlled by multiple ligand/receptor systems. Upon activation, receptors transduce the signal to effector proteins mainly Rho GTPase regulators, GTPase activating proteins (GAPs), and guanine nucleotide exchange factors (GEFs). Rho GTPases present a dominant group of regulatory proteins involved in axon guidance. In the active state, Rho GTPases recruit downstream cytoskeletal effectors to regulate the propagation and steering of the growth cone. ROCK, Rho kinase; MLCK, myosin light chain kinase; LIMK, LIM domain kinase; SRGAP, slit-robo GAP; ARP2/3, actin related protein 2/3; ENA/VASP, enabled/vasolidator-stimulated phosphoprotein. Adapted from [8].

Downstream regulators of Rho family GTPases

Rho GTPases directly or indirectly employ actin-binding proteins to modulate actin dynamics. The group of proteins that stimulate the growth of F-actin filaments can be represented by three proteins, each of which belongs to a different class of actin regulators.

The ARP2/3 protein complex (actin reacting protein) was found in high abundance at the centers of F-actin nucleation and at the branching points of actin. Furthermore, the Mena protein of the ENA/VASP family of actin binding proteins colocalizes with the ARP2/3 complexes and has been shown to be necessary for its activity [23]. Both the ARP2/3 complex and proteins from the ENA/VASP family act as the main downstream effectors of RacI Rho GTPase promoting actin polymerization. The ARP2/3 complex has also been shown to be indirectly regulated by CDC42 Rho GTPase through N-WASP (neural-Wiskott-Aldrich syndrome protein) [24]. In addition to the role of ENA/VASP proteins in nucleation, they are believed to be responsible for the correct geometry of actin filament networks within lamellipodia. They bind to the leading edges of F-actin to stimulate its elongation. This was confirmed in ENA/VASP-deficient cells where the lamellipodia actin network contained shorter and more branched filaments [25].

Another important mechanism for actin polymerization is the stabilization of novel F-actin filaments through actin bundling. One of the most prominent actin-bundling proteins is fascin, which is highly enriched in filopodia, but has relatively low abundance in lamellipodia [26]. This corresponds to the need for more massive and linear structured actin filaments in radially oriented filopodia rather than in a lamellipodia network. A reduced association of fascin with the actin filament has also been observed in the proximal part of filopodial F-actin in the T zone, where actin depolymerization occurs [26, 27]. Fascin regulation is again very complex, further accentuating its importance. Localized promotion of fascin-related actin-bundling activity by Rho GTPases was described for RacI and CDC42 [28] and more recently for the RhoA GTPase-mediated ROCK-LIMK pathway [29].

The group of downstream effectors of RhoA GTPase also contains other proteins involved in the regulation of the growth cone cytoskeleton machinery, such as myosin II, an actin motor protein required for the proper function of actomyosin contraction and retrograde F-actin flow [15], or actin depolymerization factor/cofilin (ADF/cofilin), family of actin-severing proteins [7].

One of the most important proteins regulated by RhoA GTPase is the RhoA kinase (ROCK). Upon activation, ROCK can phosphorylate several downstream targets, including myosin light kinase [15], which induces myosin II activity, ezrin-radixin-moezin proteins [30], and LIMK [31]. ADF/cofilin was shown to be regulated by LIMK-facilitated phosphorylation on the Ser-3 residue. This phosphorylation prevents it from binding to actin filaments and therefore results in a slowdown of F-actin disassembly [26]. ADF/cofilin activation is provided by slingshot phosphatase, which dephosphorylates the serine residue of ADF/cofilin, allowing its binding to F-actin [31]. The function of ADF/cofilin in the growth cone was identified as essential for the retrograde flow of F-actin, as it is the main driving force of actin turnover [32, 33]. ADF/cofilin has an affinity for ADP/F-actin higher than that for the novel ATP/F-actin, leading to preferential colocalization with the pointed end of actin filaments in the T zone, since polymerization of F-actin takes place nearly exclusively at the leading edge of growth cones [32, 34].

1.2.3 Molecular mechanism of axon guidance

Growth cones must be carefully guided through a system of extracellular signals. Each of these signals interacts with its cognate receptor on the membrane of the growth cone. The interplay between signals from multiple cue-receptor systems results in a distinct change in the dynamics of the growth cone cytoskeleton, steering the growth cone in the intended direction. Among others, netrins, slits, semaphorins, and ephrins are the most conserved and best-understood guidance cues.

Netrins, DCC and UNC-5

Netrins were first discovered in chicken brain tissue as homologues of UNC-6, a protein involved in axon guidance in *C. elegans* [35]. Netrins are 60-80 kDa proteins secreted in the extracellular space where they activate the DCC and UNC-5 receptors in the growth cone membrane (Fig. 1.3, page 18) [35, 36]. Although netrins were first described as chemoattractants, they can also act repulsively through the formation of UNC-5:DCC heterodimeric receptor complexes in different types of axons [37]. Similarly, the formation of a DCC homodimer upon binding to the ligand is necessary for the attractive effect of netrins [38]. Whether exposure of the growth cone to netrins will result in its attraction or repulsion is regulated by many factors, including netrin concentration, UNC-5 receptor membrane level, or second messenger signaling [38]. Furthermore, DCC receptors are activated upon phosphorylation by Fyn tyrosine kinase and MARCKS (myristoylated alanine-rich C-kinase) on tyrosine residues. Both kinases were necessary for receptor function when studied in knockout mice [39, 40].

Slits and Roundabout

Slits are a group of large glycoproteins of 200 kDa involved in axon guidance, as well as in axon branching [41]. They act through roundabout receptors (Robo) (Fig. 1.3, page 18) and can exhibit ambiguity in signaling similar to netrins, as they can prevent axons from crossing the midline during nervous system development [42] but also act as an attractant and promote branching in other cases [41]. Slits are generally secreted, but can also be associated with the extracellular matrix or the cell membrane [43]. Robo receptors and slits are processed by proteases, and the proteolytic regulation was found to be essential for their signaling. Binding of the slit to Robo1 leads to conformational changes and exposure of a metalloprotease cleavage site in the juxtamembrane domain of the receptor. Subsequent cleavage at this site is required for further activation of downstream signaling molecules [44]. The slits also contain a metalloprotease cleavage site conserved from *Drosophila* to vertebrates. Cleavage results in two forms of slit, one large slit-N (containing the N-terminal part) and one short slit-C (containing the C-terminal part) [45]. The slit-N and the full-length slit are both able to activate Robo receptors and tend to associate with the cell surface. Interestingly, slit-C is predominantly present in the extracellular space and has been shown to bind to the plexin A1 receptor and induce the collapse of the growth cone of the commissural axons [43, 45].

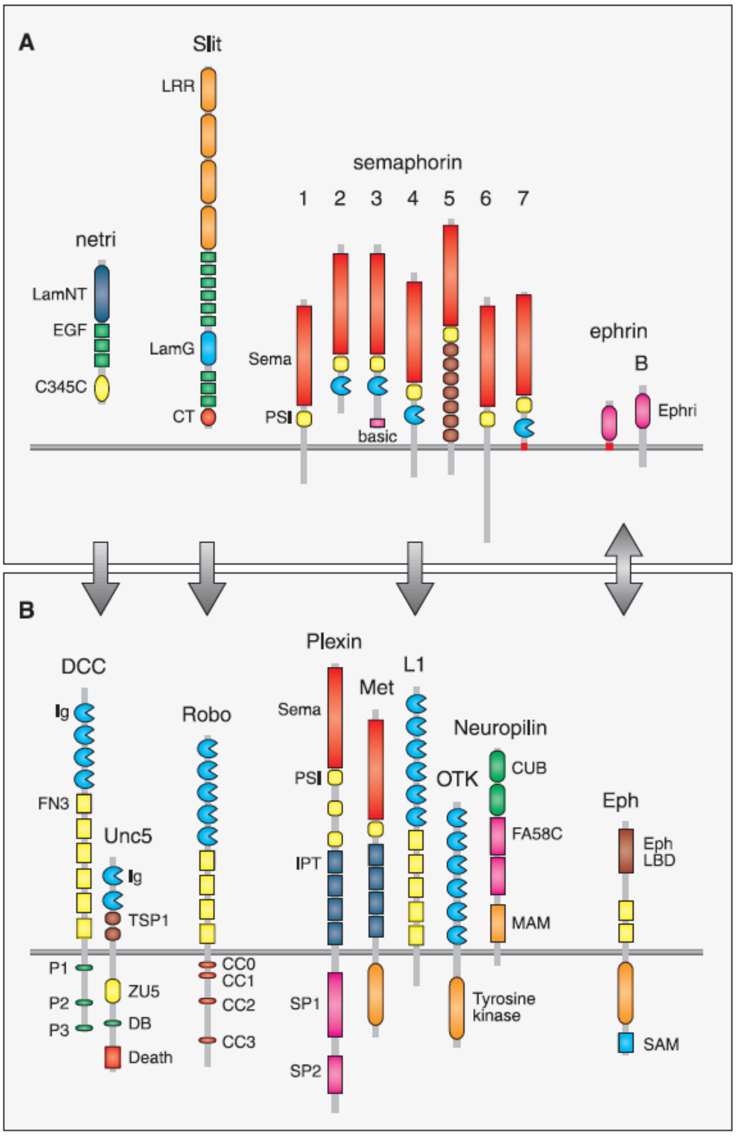

Figure 1.3: ***Signaling molecules involved in axon guidance A) and their receptors B)***
Receptors: DCC, deleted in colorectal carcinoma; UNC5, uncoordinated protein 5; Robo, roundabout; OTK, off-track tyrosine receptor kinase
Protein domains: Ig, immunoglobulin domain; PSI, plexin-semaphorin-integrin domain; IPT, Ig domain shared by plexins and transcription factors. Adapted from [46].

Ephrins and Eph

Ephrins are a group of cell membrane-bound guidance molecules. They are further divided into two classes on the basis of their interaction with the membrane. Ephrin As are bound through a glycophosphatidylinositol (GPI) anchor, while Ephrin Bs are transmembrane proteins with a small intracellular domain and a transmembrane segment formed by a single α-helix (Fig. 1.3, page 18) [47]. Their receptor counterparts, Eph receptors, belong to a large group of receptor tyrosine kinases (RTKs). In the human genome, there are nine Eph receptors that bind Ephrin A ligands and five Eph receptors that bind Ephrin B ligands. Eph receptors exhibit a high level of promiscuity and can also act as Ephrin ligands in reverse signaling facilitated by the intracellular domain of Ephrin Bs [48]. On the cell membrane, Eph receptors form multimeric clusters, depending on the type of receptor, ranging from oligomeric to large multimeric complexes. The composition of these clusters can modulate the overall outcome of their signaling, as different ratios between the types of Eph receptors involved in the clustering were observed to enhance further the complexity of the response to the Ephrin signal [48, 49]. Reverse signaling of Ephrins (Eph:Ephrin) can also occur simultaneously with forward signaling (Ephrin:Eph). This was described for motor-axon navigation, where both Ephrins and Eph are expressed in the growth cone membrane [50].

Semaphorins

Semaphorins are secreted, transmembrane or GPI-anchored proteins with signaling properties that are involved in several cellular mechanisms and are therefore essential for the development and function of many systems of the body, including the cardiovascular, immune, hepatic, muscoskeletal, renal, reproductive, respiratory and nervous systems [51]. To date, almost 30 semaphorins have been identified [52]. They are divided into eight classes, based on their amino acid identity and structural characteristics. Classes 1,2 and Sema-5c can be found in invertebrates, and classes 3-7 (excluding Sema-5c) consist of vertebrate semaphorins (Fig. 1.3 A, page 18) . The eighth class, known as class V, contains two subclasses of semaphorin-like proteins that can be found in viruses [52]. Semaphorins of classes 2 and 3 are secreted proteins, while other classes of semaphorin contain transmembrane proteins, with the exception of class 7 semaphorins that are linked to the membrane through the GPI-anchor [53].

All semaphorins share an extracellular domain of approximately 500 amino acids called the sema domain (from **sema**phorin). It is not surprising that the sema domain was identified as essential for semaphorin signaling. Specifically, a 70 amino acid region in Sema3A (166-235) was sufficient to cause the collapse of the growth cones of the dorsal root ganglion [54]. Furthermore, several residues of the homologous region in *Drosophila* Sema-2a (180-252) were identified to be responsible for the specificity of binding to different Plexin receptors [55]. Following the sema domain, semaphorins, with the exception of some viral semaphorins, contain a plexin-semaphorin-integrin (PSI) domain. This cysteine-rich region forms a cysteine knot structure and is conserved in semaphorins, plexins, integrin-β

and the MET receptor [56]. Classes 2-4, 7 and V also share an immunoglobulin domain, which can increase the impact of semaphorin signaling, as observed for Sema3A [54].

Unlike other classes of semaphorins, class 5 semaphorins contain the thrombospondin domain, which allows them to interact with the glycosaminoglycan portion of chondroitin sulfate and heparan sulfate proteoglycans (CSPGs and HSPGs, respectively). Interaction with HSPGs is necessary for the attractive activity of Sema5A, while interaction with CSPGs alters the chemoattractive activity of Sema5A to a repulsive signal [57]. Interestingly, although Sema3A lacks the thrombospondin domain, it colocalizes with proteoglycans in the extracellular matrix. This interaction also showed to enhance the chemorepulsive activity of Sema3A [58].

Semaphorin receptors

Although plexin receptors are considered as principal receptors for semaphorins, other membrane-bound proteins acting as coreceptors, or independent receptors are often recruited, broadening the spectrum of cellular responses to semaphorin signaling. The binding of class 3 semaphorins to plexin As is facilitated by neuropilin-1 (Nrp-1), a membrane protein that does not directly transduce the signal, but rather stabilizes the Nrp-plexin interaction [59]. Similar mechanisms based on the formation of heteromeric receptor complexes were also observed with receptor tyrosine kinases, OTK (Sema-1a:PlexA), MET and ErbB-2 (Sema4D:plexinB1) [60, 61, 62], the L1 immunoglobulin superfamily neural cell adhesion molecule (NrCAM) together with Nrp-2 (Sema3B/F) [63] and L1 immunoglobulin superfamily cell adhesion molecule (IgCAM) together with Nrp-1 (Sema3:plexinA1) [64].

Plexins

Plexins are a group of transmembrane receptors with a genetic link to semaphorins. There are four classes of vertebrate plexins A-D with 9 members, plexinA1-4, plexinB1-3, plexinC1, and plexinD1. They are type I transmembrane proteins with a large ectodomain that contains the ligand-interacting sema domain and several repeats of the PSI and IPT domains (Ig domain shared by Plexins and Transcription factors), the number and order of which differs between Plexin classes (A–D) [65]. The single pass-through transmembrane region is predicted to be α-helical and the protein ends with a 600 amino acid long cytoplasmic region. In the cytoplasm, plexin forms the GAP and Rho GTPase binding domains (RBD), where the RBD sequence is inserted between the two halves of the GAP domain topology. Although this arrangement is unusual, the GAP domain retains its structural resemblance to typical cytoplasmic GTPase activating proteins such as α-chimerin or SRGAP [56].

Semaphorin-plexin signaling

Semaphorin-plexin signaling in invertebrates is facilitated by four semaphorins and two plexin receptors, Sema-1a and Sema-1b bind to PlexA and Sema-2a and Sema-2b bind to PlexB [51]. When studied in *D. melanogaster*, all invertebrate semaphorins, except for Sema-2b, which possessed chemoattractive properties, promoted repulsive axon guidance [66]. The receptor complex for Sema-1a signaling also contains the receptor tyrosine kinase OTK, which modulates the repulsive effect of Sema-1a [60]. Activation of the PlexA receptor allows interaction of the cytoplasmic domain with several specific downstream effectors. PlexA can bind Nervy, an anchoring protein for A-kinases, which couples PlexA to type II protein kinase A activity [67] and also flavoprotein monooxygenase MICAL (molecule interacting with CasL) [3]. On the other hand, the PlexB GAP domain can activate RhoA and Rac GTPase activity [68].

Although semaphorin-plexin signaling in vertebrates is much more complex, general principles are conserved. As already mentioned, for interaction with class 3 semaphorins, plexinA receptors form heteromultimeric complexes with Nrp-1 or Nrp-2 and can recruit IgCAM for further differentiation of signaling [68]. Unlike other class 3 semaphorins, Sema3E binds directly to plexinD1, without the need for Nrp. However, binding of Nrp-1 to plexinD1 changes its repulsive signaling to attraction [69]. Other classes (4-7) of vertebrate semaphorins also bind directly to plexin receptors but may also utilize other coreceptors, such as MET or ErbB2 (Sema4D:plexinB1) only for signaling [68].

Downstream effectors of semaphorin-plexin signaling

Although numerous downstream effectors of plexin-linked receptor tyrosine kinases have been described, less is known about effectors that interact directly with the cytoplasmic domains of vertebrate plexins. In one of the first studies, plexinA1 has shown to be associated with Rho GEF FARP2 [70]. Upon binding of Sema3A to Nrp-1:plexinA1, FARP2 is released and activates Rac1 GTPase by its GEF activity. Rac1 activation leads to binding of Rnd1 to plexinA1 RBD, which was thought to subsequently induce plexin GAP activity to negatively regulate R-Ras through the plexin GAP domain [70]. However, the role of R-Ras in plexinA signaling is questionable, as further studies showed that the GAP domain exhibits GAP activity for Rap GTPase rather than for R-Ras [71]. Furthermore, the GAP activity of the GAP domains of plexinA1 and plexinB1 appears to be released by dimerization of the cytoplasmic domains of the plexin receptor induced by semaphorin binding. The activated plexin GAP domain then specifically inactivates Rap GTPase, which is an upstream effector of RhoA GTPase [72]. Moreover, Rap GTPase also binds to p120-RasGAP, reducing its GAP activity. As p120-RasGAP regulates the activity of several Ras GTPases, including R-Ras, inactivation of Rap1 induced by PlexA1 signaling will also result in the deactivation of R-Ras [73]. Therefore, Ras inactivation is caused by the downstream effects of Rap inactivation rather than by direct interaction with the plexin GAP domain. Interestingly, Rnd1 GTPase, which binds to RBD in the plexin cytoplasmic region, is necessary for semaphorin-plexin signaling *in vivo* [70, 73] and can even trigger plexin signaling in the absence of semaphorins [74]. Despite these observations, the exact mechanism of plexin Rnd1-mediated activation remains elusive [75, 76].

The dimerization model of the activation mechanism was more recently strengthened by structural studies showing that the inactive state of plexinA receptors is caused by cis-interaction between receptor ectodomains. This interaction prevents contact between the cytoplasmic regions of the plexins that is necessary for Rap binding [65, 72]. Furthermore, a novel study, using molecular dynamics simulation, presents a functional mechanism of Rnd1-mediated dimerization of plexin [77]. Binding of Rnd1 to RBD stabilizes the plexin dimerization interface of the juxtamembrane helices, which facilitates dimerization with another Rnd1-bound plexin. Simultaneously with dimerization, conformational changes at the active site of the GAP domain enable the binding of Rap GTPase [77].

Regulation of the activity of RhoA, Rap, Ras GTPases or FARP2, controlled by semaphorin-plexin signaling, affects various intracellular processes. Reduced activity of Ras GTPases as a consequence of Rap deactivation leads to inactivation of collapsin response mediator protein 2 (CRMP-2)[78], which is associated with promotion of microtubule polymerization through binding to tubulin heterodimes [79]. In addition, Rap also regulates RhoA GTPase, which is responsible for the regulation of F-actin polymerization as it activates ROCK [80] which is an upstream regulator of ADF/cofilin [26] and myosin II [15]. Therefore, Rap inactivation leads to stalling of F-actin elongation and may be essential for semaphorin-mediated collapse of the growth cone [71]. Furthermore, inactivation of Ras proteins together with FARP2 activation has a direct negative impact on integrin-mediated cell adhesion [70, 81].

Another important mechanism of semaphorin-plexin signaling is the activation of MICAL proteins. MICAL proteins interact directly with the cytoplasmic region of plexinA receptors through their C-terminal domain [3] and although no direct association of MICAL with plexinBs has been observed, *Drosophila* PlexB signaling is also MICAL dependent [82]. MICAL interaction with plexinA leads to the release of the autoinhibition state of MICAL [83, 84]. Activated MICAL disassembles F-actin filaments through the oxidation of F-actin subunits and is therefore essential for axon repulsive signaling of semaphorins [4]. Furthermore, MICAL also forms a complex with plexin and CRMP-2 and may play a role in the activation of CRMP-2 [84].

1.3 MICAL proteins family

MICAL protein family is a small group of proteins conserved in multicellular organisms with monooxygenase function facilitated by a flavin monooxygenase domain. There are three paralogous genes that encode MICAL proteins in vertebrates, *MICAL 1-3*, and one gene *MICAL* in invertebrates. The name of the group stands for Molecule Interacting with CasL, which corresponds to the first observation of the MICAL protein. This was done by *Suzuki et al.* in 2002 in complex with CasL, a highly phosphorylated protein expressed in lymphocytes, where it acts as a signaling molecule in the β_1 integrin pathway [85]. Immediately after its discovery, the function of MICALs was linked to a semaphorin-plexin-mediated axon repulsion pathway in neurons [3]. MICAL proteins are primarily related to the regulation of actin filament disassembly during axon guidance, but also appear to exert different cellular effects through interaction with other proteins such as exocytosis, cytokinesis, or apoptosis [86, 87].

1.3.1 MICALs and diseases

In recent years, researchers have discovered that deregulation of MICAL genes and overexpression of *MICAL* genes in cells are often associated with cancer progression and neurodegenerative diseases [6, 88, 89, 90]. Several mutations in the *MICAL 1* gene were related to autosomal dominant lateral temporal epilepsy (ADLTE). Specifically, the substitution for G150S (p.Gly150Ser) located in the monooxygenase domain and the frameshift indel (p.Ala1065fs) in the C-terminal domain. When studied in COS-7 cells, both mutations led to increased MICAL-1 monooxygenase activity and induced cell contraction [5]. Furthermore, down-regulation of MICAL-2 expression is associated with anxiety behaviors and neuropathology in certain neuropsychiatric disorders [91]. Therefore, MICAL-2 may serve as a potential therapeutic target for the treatment of neuropsychiatric diseases.

1.3.2 Structure of MICAL proteins

Human MICAL-1 is 1067 amino acids long and its structure consists of five conserved domains (Fig. 1.4, page 24). N-terminal flavin monooxygenase domain (MO domain, residues 1-489 of human MICAL-1 unless stated otherwise), followed by the Calponin homology domain (CH domain, residues 510-613) and the LIM domain (residues 688-756), which is connected via a short linker region (residues 635-679). Before the C-terminal region, we find two conserved motifs, the proline-rich PPKP motif (residues 830-833) known for its interaction with the Src homology 3 (SH3) domain of the CasL protein [85] and the glutamic acid-rich region (residues 866-881) of yet unknown function. The C-terminus consists of a highly conserved coiled-coil domain (residues 918-1067), also called the Rab binding domain for its ability to bind proteins from the Rab family [92, 93].

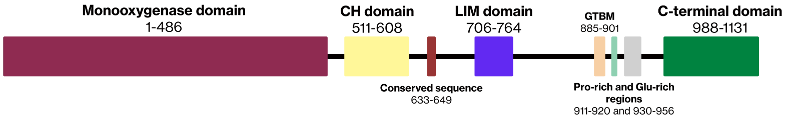

Figure 1.4: ***Structure of full-length MICAL-1 from Coturnix japonica***
Scheme of MICAL-1 primary sequence shows the organization of domains. Other conserved regions, minimal Myosin Va^{GTD} *binding motif (GTBM, light orange), newly identified conserved sequence between the CH and LIM domains (ruby), the proline-rich region (green cyan) and the glutamic acid-rich region (white), are also shown.*

Sequence analysis showed that, opposite to MICAL-2 and MICAL-3, MICAL-1 lacks a nuclear localization signal, a RKRX$_{14}$KRRK sequence positioned between the CH and LIM domains in MICAL-3 (residues 633-683 of human MICAL-3). This was confirmed by a subcellular localization study of MICALs in HEK293T cells where MICAL-2 and MICAL-3 were localized in the nucleus. However, MICAL-1 was predominantly localized in the cytoplasm [94]. Another important difference between human MICAL forms is the absence of the C-terminal domain in the MICAL-2 sequence, which is believed to be responsible for the interaction with several proteins, and is supposed to play a crucial role in the autoinhibition mechanism of MICAL-1 and MICAL-3 [3, 84, 85]. However, some motifs that are necessary for interaction with typical MICAL interaction partners, such as Rab1 and CasL, are conserved at other sites in the MICAL-2 sequence [92, 94, 95, 96].

Monooxygenase domain

High-resolution crystal structures of the murine MICAL-1 MO domain were subsequently solved by *Siebold et al.* [97] and *Nadella et al.* [98] in 2005. The monooxygenase domain of MICALs is a flavin-containing monooxygenase with close resemblance to para-hydroxybenzoate hydroxylase (pHBH) and NADPH-dependent enzymatic activity. It is made up of two nonidentical subdomains, the FAD binding subdomain and the monooxygenase subdomain [97, 98]. The FAD binding subdomain consists of two sequences, residues 1-226 and 373-484, with three specific motifs that form the FAD binding pocket (Fig.1.5, page 25) [98]. These are Rossman $\beta-\alpha-\beta$ fold (residues 84-114), a supersecondary structure that frequently occurs in flavin NADPH-dependent oxidoreductases, important for binding to ADP of flavin adenine dinucleotide, a conserved DG sequence (residues 212-225) binding the pyrophosphate moiety of FAD, and GD motif (residues 386-416) contacting the ribose moiety [99]. The monooxygenase subdomain is connected to the FAD binding subdomain through a long antiparallel $\beta-$sheet. The ribitol moiety of the FAD molecule is buried within the FAD-binding subdomain, whereas the isoalloxazine ring is exposed at the active site formed in the interaction space of the two subdomains. In the oxidized state, the isoalloxazine ring adopts a planar conformation stabilized by hydrogen bonds of N123 and Y293 with the N5 and O4 of the isoalloxazine ring, respectively [97]. This so-called "out" conformation is perturbed upon the reduction of FAD through oxidation of NADPH, which leads to a switch to the "in" conformation of the reduced isoalloxazine ring. In response to the conformational change of the FAD, the monooxygenase subdomain reorients to form a channel that leads directly to the active site. This channel can serve as an access point to the amino acid side chain of the substrate [97].

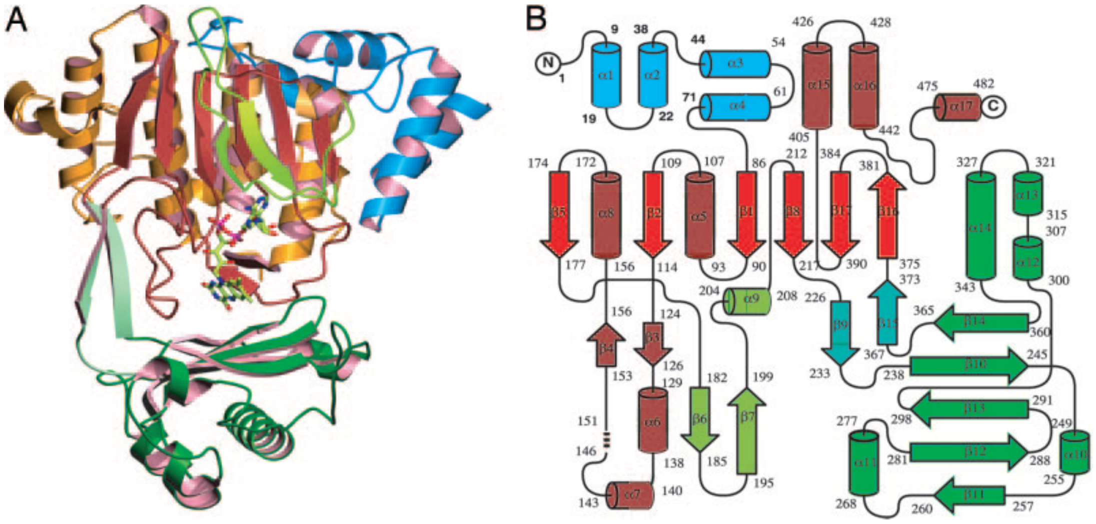

Figure 1.5: ***Monoxygenase domain of murine MICAL-1***

A) Ribbon representation model of the MICAL-1 monooxygenase domain. The monooxygenase subdomain, colored green/pink, is connected to the FAD binding subdomain through an antiparallel beta sheet (palegreen). The FAD molecule is displayed in the "out" position of reduced flavin.

B) Schematic representation of the structure of the MICAL-1 monooxygenase domain. Secondary structures involved in FAD binding are $\beta1$,$\alpha4$,$\beta2$ (Rossman fold, residues 84-114), $\beta8$ (DG sequence, residues 221-225) and residues 386-416 of $\beta17$ and $\alpha15$ (GD motif). Adapted from [98].

Calponin homology domain

Calponin homology (CH) domains are conserved in a wide variety of actin-interacting proteins. There are five types of CH domain, while typical actin-binding proteins such as α-actinin or β-spectrin contain a set of one CH type I domain (CH1) followed by a type II domain (CH2). The role of CH2 in actin binding has not yet been fully understood as, unlike CH1, it has only a low affinity for F-actin [100]. Interestingly, MICAL proteins contain only one type II CH domain [101].

The structure of the CH domain of MICAL-1 is formed by six alpha helices and a 3_{10} helix folding into a distinct globular shape (Fig.1.6). Three of four longer α-helices form a parallel bundle, whereas the fourth α-helix lies almost perpendicular to them. Although the sequence identities between the MICAL-1 CH domains and other CH domains are below 50 %, the overall structure is well conserved. The lack of actin binding affinity of the MICAL-1 CH domain may be the result of the replacement of hydrophobic residues in the actin-interacting region of CH1 by more hydrophilic residues in the MICAL-1 CH domain [101]. The exact role of the CH domain of MICALs remains unknown; however, there are some implications that it may be involved in the interaction with microtubules [96] or act as an enhancer of affinity to other MICAL interaction partners, e.g. F-actin [102]. The latter is supported by observations made in several studies that focused on the enzymatic activity of MICAL-1 constructs containing an isolated MO domain or a MO-CH construct. *Hung et al.* showed that the calponin homology domain is essential for the *in vivo* activity of MICAL [83], and indeed, when studied *in vitro*, the MO-CH MICAL-1 construct manifested an activity approximately 10 times higher in the presence of F-actin than the MO domain of MICAL-1 alone [103].

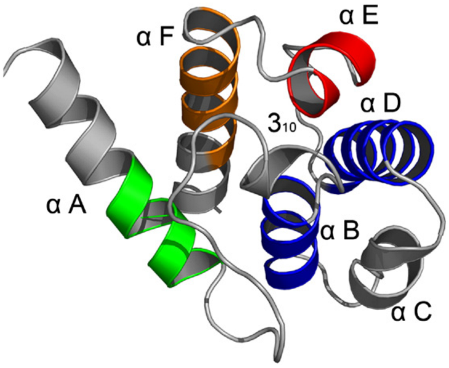

Figure 1.6: *Structure of human MICAL-1 CH domain*
Ribbon representation of the human MICAL-1 CH domain energy-minimized averaged structure solved by NMR [101]. α-helices B, D, and F are creating parallel bundle while α-helix A is 70 ° rotated. α-helices B,D and D,F are linked via short α-helices C and E, respectively. α-helices A and B are connected through 3_{10}-helix. Adapted from [104]

LIM domain

LIM domains (**L**IN-11, **I**sl1 and **M**EC-3) are found in many proteins with diverse cellular functions. Proteins containing LIM domains are involved in cytoskeleton organization, cell adhesion, gene expression regulation, and signal transduction [105]. The human MICAL-1 LIM domain is made up of 55 amino acid residues and follows a classical LIM domain consensus sequence, $CX_2CX_{17}HX_2CX_2CX_2CX_{19}CX_2H$. This primary sequence folds into two zinc finger motifs where the first four conserved C/H residues coordinate one zinc ion and the second four conserved residues coordinate the second zinc ion, creating a tandem zinc finger topology (Fig.1.7) [105]. The isolated MICAL-1 LIM domain structure was solved in solution by NMR (PDBid: 2CO8) and shows that, as in other LIM domains, the zinc fingers are treble-clef fold. Each treble-clef finger is formed by two orthogonal oriented β-hairpins followed by a short α-helix. The exact role of the LIM domain in

MICAL proteins has not yet been determined. Although LIM domains often serve as a modular protein binding interface [105], to date only one interaction partner of the MICAL-1 LIM domain has been identified, the collapsin response mediator protein (CRMP) [84]. Interestingly, the LIM domain also interacts with the C-terminal domain of MICAL and, therefore, may play an important role in the autoinhibition mechanism of MICAL-1 [84, 106].

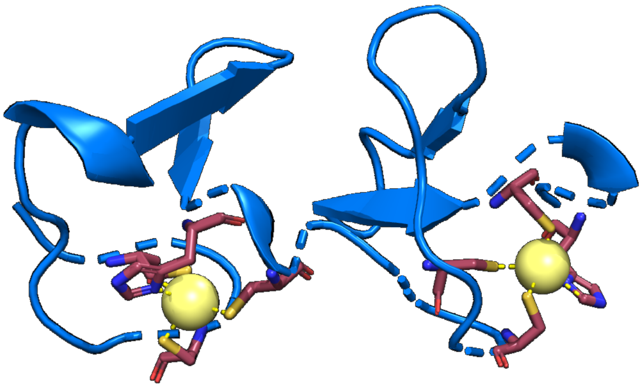

Figure 1.7: ***Model of MICAL-1 LIM domain from Coturnix japonica***
Structure was predicted by Alphafold. Residues interacting with zinc ions are colored in dark-salmon. Zinc ions are colored pale yellow. Their positions are based on the superimposition of the NMR structure of the human MICAL-1 LIM domain (PDBid:2CO8). The figure was produced with PyMol.

C-terminal domain

The C-terminal domain of MICAL-1 and MICAL-3, also known as the Rab binding domain [92], the coiled coil domain [86], or the plexin-interacting region [107], is a domain at the C-terminus of the protein made up of three α-helices that form a coiled coil motif. The domain is approximately 150 amino acids long, possibly originating from a duplication of a gene that encodes a single α-hairpin, which resulted in a structure in which the central α-helix creates a continuous connection between the two α-hairpins [108, 109] (Fig.1.8, page 28). The C-terminal domain of MICALs, as different names suggest, is known to interact with many proteins, including Rab proteins [93, 95, 96, 108, 109, 110], plexin receptor [3], vimentin [85], NDR [86], but also intramolecularly with other domains [84, 106]. The most studied interaction is with Rab proteins, where many X-ray crystallography structures have also been published showing two binding sites for Rab molecules with different affinity [108]. Analogical findings were made with Eps15-homology domain containing protein (EHBP1) that includes a C-terminal domain closely similar to that of MICAL proteins [111].

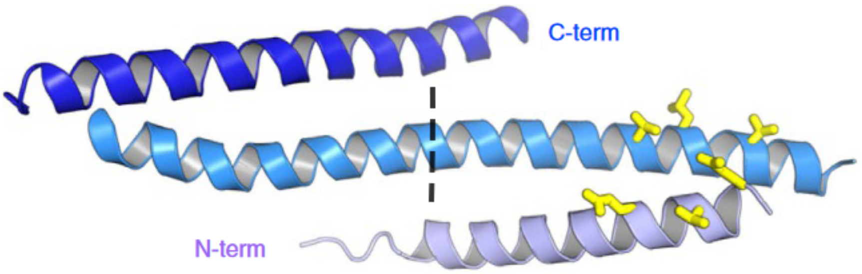

Figure 1.8: *The C-terminal domain of human MICAL-1*
Structure of the C-terminal domain solved by X-ray crystallography. It consists of three α-helices that fold into a coiled coil motif. The flexible linkers that connect the helices are not visible. Residues of one binding site involved in interaction with Rab proteins are in licorice representation and colored yellow (E946, V950, E953, V971, L975, V978). The line in the middle illustrates the symmetry of the structure, probably originating from the evolution of the domain by gene duplication. Adapted from [109].

Other conserved regions

The interdomain regions or linker regions of the MICAL proteins are mainly disordered (based on the prediction of the structure by AlphaFold), which also explains why the complete structure of MICAL has not yet been solved. Nevertheless, they contain several conserved regions that may form a stable structure under certain conditions or within protein-protein interactions. This was recently confirmed in the publication that presents the Myosin Va motor in complex with the newly identified minimal Myosin VaGTD binding motif (GTBM) located in the loop between the LIM and the C-terminal domain of MICAL-1 (residues 800-822) [112]. It remains to be elucidated whether other conserved regions such as, the proline-rich region, containing the SH3 domain binding motif (residues 830-833), or the glutamic acid-rich region (residues 866-881), are capable of folding into a stable structure.

1.3.3 MICAL function

MICAL catalyzes oxidative disassembly of F-actin

The MICAL oxidation of methionine residues presents a novel mechanism of F-actin depolymerization. MICAL catalyzes the specific hydroxylation of M44 and M47 of *Drosophila* actin subunits. The residues M44 and M47 are located within the D-loop of actin, a highly flexible region of 12 amino acids, which plays an important role in the actin-actin contacts necessary for actin polymerization [4]. Oxidation of these two methionine residues results in the destabilization of F-actin and subsequent catastrophic depolymerization of the F-actin *in vitro* [113]. The M44 of actin is highly conserved across species and its oxidation, not that of M47, is crucial for the destabilization of the F-actin filament [4, 113]. Furthermore, M44 mutations are responsible for myopathies associated with muscle weakening, further illustrating the importance of the oxidative mechanism of cytoskeleton remodeling [114].

Although MICAL-mediated oxidation of F-actin leads to fast depolymerization *in vitro*, for efficient depolymerization *in vivo*, MICAL cooperates with at least two other proteins, cofilin and profilin [115, 116]. Binding of cofilin to F-actin destabilizes actin filaments and is essential for the severing mechanism in the T zone of growth cones [33]. Interestingly, actin oxidation improves the affinity of cofilin to F-actin and significantly accelerates the collapse of F-actin filaments both *in vitro* and *in vivo* [115]. During F-actin polymerization, the second protein, profilin, forms complexes with G-actin to fuel F-actin polymerization in cooperation with the elongation factors Ena/VASP and formin. Similarly to cofilin, profilin has a high affinity for oxidized actin. However, the formation of profilin complexes with oxidized G-actin does not stimulate F-actin polymerization, but rather inhibits it and even further destabilizes the oxidized F-actin filament [116]. Repolymerization of actin is possible only after the oxidized actin units are reduced back by the seleno protein MsrB1 [117].

Reaction mechanism and kinetics

The monooxygenase domain of MICALs is a NADPH-dependent flavin monooxygenase with close structural similarity to pHBH. Based on the crystallographic structure of the MO domain, the FAD cofactor can adopt two specific conformations, "in" and "out". The transition between these two states is necessary for the reaction mechanism [97]. The inactive enzyme remains with the FAD in the "out" position. Upon binding of NADPH, a conformational change in the MO domain switches the FAD to the "in" position, which presents the active state of the protein. In the "in" conformation, after hydride transfer from NADPH, the isoalloxazine ring loses planarity and adopts a butterfly conformation of neutral hydroquinone. Simultaneously, repositioning of amino acid side chains at the active site opens a channel leading from the surface to the C4a carbon of $FADH_2$ [118]. The opening of the channel and the change in the conformation of the isoalloxazine ring are also the rate-limiting steps of the entire catalytic cycle [119].

In the absence of F-actin, the catalytic cycle runs through a hydrogen peroxide pathway, working as an NADPH oxidase with a K_M for NADPH in the order of hundreds of μM [119]. However, when MICAL acts in the presence of F-actin, oxygen transfer from the FAD-hydroperoxide intermediate is strictly enantioselective, indicating that the reaction mechanism involves a step of direct transfer of oxygen to the sulfur atom of methionine (Fig. 1.9, page 31) [117]. Binding of F-actin also dramatically increases the rate of NADPH oxidation, showing that F-actin acts as a non-essential activator [118]. Interestingly, even in the presence of F-actin the reaction mechanism is not completely coupled. During the oxidation reaction of F-actin catalyzed by the MO domain of MICAL-2, only a half of hydroperoxide intermediates undergoes breakage of the oxygen-oxygen bond and subsequent transfer of oxygen to the sulfur atom of the methionine residue. The other half follows the “oxidase path” and directly releases hydrogen peroxide [120]. This may be even more turned in favour of hydrogen peroxide formation in the case of MICAL-1 as it produces much higher levels of hydrogen peroxide than the other two MICAL family members [107].

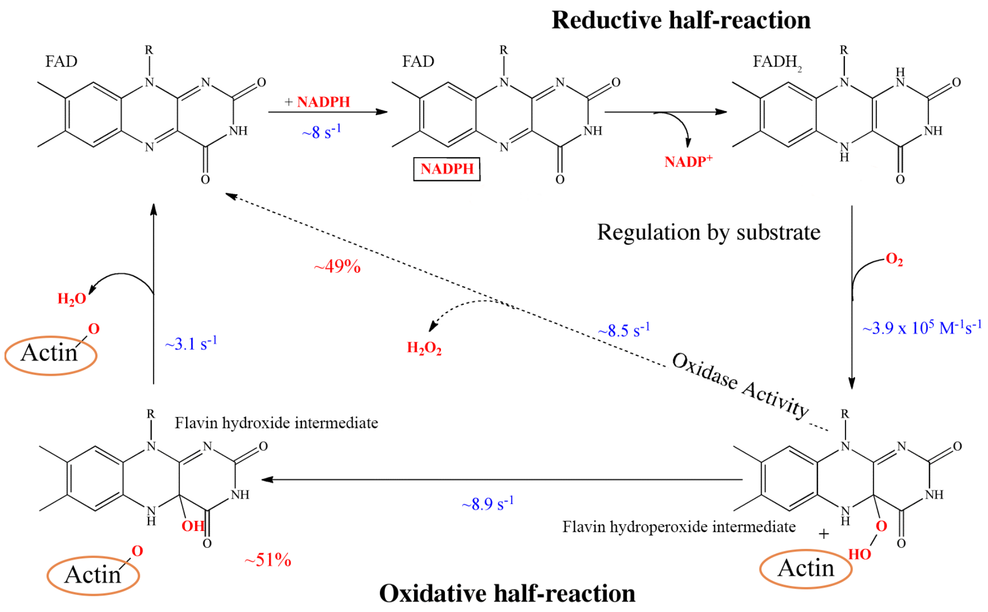

Figure 1.9: ***Scheme for the reaction mechanism of the MICAL-2 monooxygenase domain in the presence of F-actin***

FAD is first in the "out" position reduced by NADPH. Reduction triggers conformational changes, and the isoalloxazine ring creates a butterfly conformation. Binding of the oxygen molecule to the C4a carbon of flavin leads to the formation of a flavin hydroperoxide intermediate. Hydroperoxide flavin can undergo either a shunt, releasing hydrogen peroxide or breakage of the oxygen-oxygen bond leading to flavin hydroxide and methionine sulfoxide formation. The rate constants for all reaction steps are written in blue. Adapted from [120].

MICAL interaction partners

In addition to F-actin, many MICAL protein interaction partners have been identified that include not only proteins believed to be involved in MICAL regulation, such as Rab proteins [95, 108], vimentin [85], CasL [85], plexins [84] and kinases [121], but also other cytoskeleton proteins, actin myosin motors [112, 122] and microtubules [96]. Furthermore, a recent study identified peroxidase Prx1 as a novel substrate for MICAL-1 [123].

Rab proteins are membrane-bound GTPases signaling through multiple downstream interacting molecules, regulating diverse membrane processes including the motility, formation and docking of vesicles or remodeling of cellular compartments [124]. The first identified interaction of MICALs and Rabs was between Rab1 and MICAL-1 [95] and was later expanded to the three vertebrate MICALs, together with a connection to microtubules [96]. The complex study of Rab proteins interaction partners using yeast two-hybrid screening revealed that in addition to Rab1, MICAL-1 also interacts with Rab8, Rab10, Rab13, Rab15, Rab35, and Rab36 [125]. However, MICAL-1 isothermal titration calorimetry binding assays with Rab1, Rab8, Rab10, Rab13, Rab15, and Rab35 showed complex formation only for Rab1 and Rab8 [108]. Rab1 binds to MICAL-1 with a dissociation constant of 2.2 μM, whereas Rab8 forms a complex with 2:1 stoichiometry with dissociation constants for enthalpy-driven and entropy-driven binding sites, 55.5 nM and

480 nm, respectively [108]. The link between MICAL proteins and Rab proteins that control intracellular vesicles appears to be more reasonable in light of the recently observed interaction between MICAL-1 and actin motor myosin Va [112]. Myosin Va binds to the cellular cargo and cooperates with the Spire 1/2 protein, which stimulates the assembly of F-actin for transport to the targeted location. At the destination, the Spire 1/2 is replaced with MICAL-1, MICAL is activated by interaction with the Rab protein and facilitates the unloading of the cargo by disassembling F-actin [112]. Furthermore, Rab8 was found to recruit MICAL-3 to control docking and the fusion of exocytotic vesicles with the plasma membrane. In addition to the disintegration of actin filaments, MICAL-3 was also found to be responsible for the oxidative disassembly of the vesicle coupling complexes, which is necessary for the fusion of the vesicle with the membrane [110].

Collapsin response mediator proteins are a group of cytosolic proteins involved in the polymerization of microtubules. In the active state, CRMPs bind to tubulin heterodimers and promote microtubule elongation. The activity of CRMPs is regulated through oxidation-dependent phosphorylation [126]. CRMPs are active in the reduced state. Oxidation of CRMP leads to formation of a disulfide-linked homodimer. The disulfide-linked homodimers of CRMP are captured by thioredoxin for preferential phosphorylation by the GSK-3β kinase[126]. CRMP2 oxidation was shown to be regulated through the Sema3A/Np-1/PlexinA pathway that promotes growth cone collapse [127]. Furthermore, CRMP2 binds directly to MICAL-1 in the region around the LIM domain [84], and therefore MICAL is a promising candidate for the catalysis of CRMP oxidation. And indeed, CRMP2 oxidation is dependent on the production of hydrogen peroxide by MICAL-1 [126]. However, CRMP is not directly oxidized by H_2O_2 produced by MICAL-1. Interestingly, MICAL-1 first transduces the redox signal through H_2O_2 to cytosolic peroxiredoxin 1 (Prx1), which in the next step oxidizes the cysteine residues of CRMP2 [123]. However, the mechanism of the reaction is different from MICAL-catalyzed oxidation of F-actin, since no flavin hydroxide intermediate was detected [123]. Therefore, Prx1 must be oxidized by the production of hydrogen peroxide by MICAL-1 [120, 123]. Prx1 therefore presents a second substrate for MICAL activity in addition to F-actin and reveals a novel mechanism of redox signaling.

2 Aims of the thesis

- Plasmid construction for the truncated form (1-979) of MICAL-1 from *Coturnix japonica* lacking the C-terminal domain.
- Production and purification of full-length MICAL-1 from *Coturnix japonica* and its truncated form using the baculoviral expression system.
- Determination of the oligomerization state of the MICAL-1 forms.
- Reaction kinetics analysis of NADPH oxidation catalyzed by the MICAL-1 forms in the presence and absence of F-actin.
- Structural characterization of full-length MICAL-1 from *Coturnix japonica* using X-ray crystallography, cryo-electron microscopy, and molecular dynamics simulation.
- Elucidation of the mechanism of MICAL-1 autoinhibition.

3 Materials and instruments

3.1 Instruments

- Agilent 1200, HPLC - *Agilent Technologies, USA*
- Agilent Infinity II, UV detector - Agilent Technologies, USA
- Äkta go, FPLC - *Cytiva, USA*
- Äkta start, FPLC - *Cytiva, USA*
- Analytical balances Luna - *Adam equipment, USA*
- Automatic pipette accu-jet pro - *Brand, USA*
- Automatic pipettes - *Gilson, USA*
- CellDrop cell counter - *DeNovix, USA*
- Centrifuge Avanti J-15R - *Beckman Coulter, USA*
- Centrifuge Avanti JXN-26 - *Beckman Coulter, USA*
- Centrifuge Optima XE - *Beckman Coulter, USA*
- Column Bio SEC-3 - *Agilent, USA*
- Column HisTrap FF (5ml) - *Cytiva, USA*
- Column Superdex 200 increase 10/300 GL - *Cytiva, USA*
- Crystallization hotel RI1000 - *Formulatrix, USA*
- Dropper Gryphoon - *Art Robbins, USA*
- Dropsetter NT8 - *Formulatrix, USA*
- EM ACE600, high vacuum sputter coater - *Leica, Germany*
- Electron microscope, JEM 2100-plus - *JEOL, Japan*
- Horizontal electrophoretic system - *EmbiTec, USA*
- Incubator My Temp - *Benchmark, USA*
- Laminar flow cabinet - *Telstar, Spain*
- Leica GP2, plunge freezer - *Leica, Germany*
- Magnetic stirrer - *Stuart, USA*
- NanoDrop One spectrophotometer - *Thermo Fischer Scientific, USA*
- Shodex RI-101, differential refractive index detector - *Showa Denko, Japan*
- Spark microplate reader - *Tecan, USA*

- Thermocycler T100 - *Bio-Rad, USA*
- Vertical electrophoretic system - *Invitrogen, USA*
- miniDAWN MALS detector - *Wyatt Technology, USA*
- pH meter - *Mettler Toledo, Switzerland*

3.2 Materials and chemicals

- Acetic acid 98 % - *Penta Chemicals, Czech Republic*
- Agarose - *Carl Roth, Germany*
- Ampicilin sodium salt - *Carl Roth, Germany*
- BenchMark™ protein ladder - *Invitrogen, USA*
- Cu 1.2/1.3, 300 mesh EM grid - *Quantifoil, USA*
- Cu continuous carbon, 300 mesh EM grid - *Quantifoil, USA*
- DNase I - *PanReac AppliChem, USA*
- DTT (1,4-dithiothreitol) - *Carl Roth, Germany*
- GeneJuice® - *Merck, USA*
- HEPES (4-(2-hydroxyethyl)-1-piperazineethanesulfonic acid) - *Carl Roth, Germany*
- Imidazole - *Carl Roth, Germany*
- InstantBlue® Coomasie protein stain - *Abcam, Great Britain*
- LB agar - *Carl Roth, Germany*
- LB medium - *Carl Roth, Germany*
- Library efficiency™ *E. coli* DH5-α competent cells - *Thermo Fisher Scientific, USA*
- LigaFast™ (T4 DNA ligase + 10 × ligase buffer) - *Promega, USA*
- MOPS SDS running buffer - *Invitrogen, USA*
- $MgCl_2$ - *Penta Chemicals, Czech Republic*
- NaCl - *Penta Chemicals, Czech Republic*
- NaOH - *Penta Chemicals, Czech Republic*
- Nonidet® P-40 subsitute - *G-Biosciences, USA*
- NuPAGE™ 10%, Bis-Tris, 1.0 mm, Mini Protein Gel - *Invitrogen, USA*
- NuPAGE™ LDS sample buffer 4x - *Invitrogen, USA*
- Pyrobest™ DNA polymerase - *TAKARA BIO, Japan*
- Pyrobest™ buffer II 10 × - *TAKARA BIO, Japan*

- QIAprep Spin Miniprep Kit - *Qiagen, Germany*
- QIAquick PCR & Gel Cleanup Kit - *Qiagen, Germany*
- SIGMAFAST™ protease inhibitor cocktail tablets - *Merck, USA*
- Sf-900 II serum free medium - *Thermo Fisher Scientific, USA*
- TCEP-HCl (tris(2-carboxyethyl)phosphine hydrochloride) - *VWR, USA*
- Tris hydrochloride - *Penta Chemicals, Czech Republic*
- Uranyl formate 99 % - *Electron Microscopy Sciences, USA*
- dNTP Mixture - *TAKARA BIO, Japan*

3.3 Used solutions and buffers

- AEX elution buffer - 15 mM Tris-HCl (pH 8.0), 1 M NaCl, 2 mM DTT
- AEX loading buffer - 15 mM Tris-HCl (pH 8.0), 10 mM NaCl, 2 mM DTT
- Actin polymerization buffer - 50 mM Tris-HCl (pH 7.5), 500 mM KCl, 20 mM $MgCl_2$, 10 mM ATP, 5 mM DTT
- F-buffer - 9 mM Tris-HCl (pH 8.0), 0.18 $CaCl_2$, 45 mM KCl, 1.8 mM $MgCl_2$, 1.1 mM ATP, 1.3 mM DTT
- G-buffer - 5 mM Tris-HCl (pH.8.0), 0.2 mM $CaCl_2$, 0.2 mM ATP, 1 mM DTT
- IMAC Binding buffer - 30 mM HEPES (pH 8.0), 500 mM NaCl, 10 mM imidazole
- IMAC Elution buffer - 30 mM HEPES (pH 8.0), 500 mM NaCl, 150 mM imidazole, 2 mM DTT
- IMAC Wash buffer - 30 mM HEPES (pH 8.0), 500 mM NaCl, 50 mM imidazole, 2 mM DTT
- Lysis buffer - 30 mM Tris-HCl (pH 8.0), 500 mM NaCl, 20 mM imidazole, 3 mM DTT, 10 mM $MgSO_4$, 1% NP-40, SigmaFast™ protease inhibitor (1 tablet), 3 mg DNAse
- SEC buffer - 15 mM Tris-HCl (pH 8.0), 150 mM NaCl, 2 mM DTT

4 Methods

4.1 Multiple sequence alignment

For the analysis of conserved regions, 286 amino acid sequences of MICAL-1 from different species were aligned using the Clustal Omega online tool [128]. The alignment file was used to calculate the conservation score at each position using the ConSurf Server [129] with the qMICAL AlphaFold pdb file as a reference (see 4.8.1). Furthermore, pairwise alignments of full-length human MICAL-1 and qMICAL-1, and also separate alignments for domains (MO, CH, LIM, C-terminal) were performed in SnapGene using the BLOSUM62 matrix.

4.2 Cloning of the truncated form of qMICAL

4.2.1 Primer design

For the expression of the truncated form of qMICAL (residues 1-979), two primers were designed for DNA amplification by PCR and to introduce restriction enzyme sites for restriction cloning (1). The forward primer was 27 bases long containing a BamHI restriction site at the 5' end, followed by three nucleotides (5'-TAT-3') to increase affinity for the BamHI enzyme. The reverse primer was 67 bases long including a 8×His-tag connected to protein by a GS linker (5'-GCTTCC-3') and a PacI restriction site at the 3' end, again followed by three nucleotides (5'-ATA-3').

Table 1: ***Nucleotide sequences of designed primers for cloning of the truncated form of qMICAL into the pBAKPac9 vector***
Nonannealed parts of sequences are in ***bold****, restriction enzyme sites are in* ***bold italics***

Primer	**Nucleotide sequence**
Forward primer	5'-**TAT*GGATCC***ATGAGTGCACCCGATGAG-3'
Reverse primer	5'-**ATA*TTAATTAA*TGGTGGTGATGGTGATGATG**-
	-**ATGGCTTCC**CCAGGTGGGGTACTTCTCTGTG-3'

4.2.2 Restriction cloning

The pBacPAK9 plasmid containing the cloned full-length qMICAL sequence was used as a template for a PCR with the two newly designed primers, to amplify the DNA coding the truncated form of qMICAL. The amplification reaction consisted of 30 μl ultrapure water, 5 μl 10 × Pyrobest™ buffer II, 4 μl of the dNTP mixture (4 μM), 5 μl of each forward and reverse primers (5 μM solutions in H_2O), 1 μl of the template DNA (concentration 1 ng/μl), and 0.25 μl of Pyrobest™ DNA polymerase. PCR was started with initial denaturation at 98 °C for 1 minute followed by 30 PCR cycles with 10 s long denaturation phase (98 °C), 30 s annealing phase (50 °C) and 3 minutes extension phase (72 °C).

The PCR product was further cleaned and cleaved with BamHI and PacI restriction enzymes, cleaned using agarose gel electrophoresis. The empty pBacPAK9 vector was first cleaved by the BamHI and PacI restriction enzymes for 8 hours at 37 °C and separated from the excised part by agarose gel electrophoresis. The gel band containing the plasmid was cut out by a scalpel and DNA was purified using the QIAquick PCR & Gel Cleanup Kit. Purified PCR product was ligated into a digested pBacPAK9 vector using LigaFast™ rapid DNA ligation system.

The ligation mixture was used for heat-shock transformation of *E. coli* DH5-α competent cells following the standard protocol [130]. Transformed cells were spread on a lysogeny broth (LB) agar plate with ampicilin using an L-shaped cell spreader and incubated overnight at 37 °C. Five colonies were picked and used for inoculation of 5 ml of LB medium with ampicilin. Cell cultures were grown for 13 hours at 37 °C and DNA was purified using the QIAprep Spin Miniprep Kit. The purified plasmid DNA was first verified by digestion using EcoRI restriction enzyme and positive clones were sent for DNA sequencing.

4.3 Expression and purification of protein

4.3.1 Maintaining the cell culture

The full-length qMICAL and its truncated form were expressed in *Spodoptera frugiperda* cells from the Sf9 cell line. The cells were grown in serum-free medium, which is derived from the pupal ovarian tissue of *S. frugiperda.* Cells were always passaged when their concentration reached a value between $4{\times}10^6$ and $6{\times}10^6$ cells/ml (approximately twice a week). 50 μl of cell stock was first diluted by a factor of four with the serum-free medium (Sf-900 II SFM) and cell density was measured. This value was used for calculation of the ratio needed for dilution of cell stock to $0.6{\times}10^5$ cells/ml. The medium and cell stock were mixed in the required ratio and incubated at 27.5°C (125 rpm) until next passaging.

4.3.2 Baculovirus transfection and viral amplification

The transfection of Sf9 cells was done using BacMagic™-3 DNA Kit. The Sf9 cells for transfection were seeded in 6 well culture plates by adding 2 ml of Sf9 cell suspension at a concentration of approximately 6×10^5 cells/ml into each well. After 1 hour incubation at 27.5°C, the excess medium was removed from the wells and 1 ml of co-transfection mixture was added. The mixture consisted of 5 μl BacMagic-3 DNA, 500 ng transfer plasmid with full-length qMICAL or truncated qMICAL DNA, 5 μl Insect GeneJuice® Transfection Reagent and 200 μl serum free medium (Sf-900 II SFM), which was previously preincubated at room temperature for 20 min. Cells were incubated for 5 days at 27.5°C. Following incubation, the medium containing virus particles was harvested and centrifuged for 10 min at 3,000×g. The supernatant was removed and later used as a P1 virus stock for viral amplification.

For viral amplification, 1 ml of the P1 virus stock obtained in the previous steps was added to a cell culture flask containing 100 ml of Sf9 cell suspension at a concentration of approximately 1×10^6 cells/ml and incubated for 1 week at 27.5°C (125 rpm). After incubation, the cell suspension was split in half and centrifuged for 10 min at 3,000×g. The supernatant was collected and about 100 ml of P2 viral stock was collected in total. Infection was carried out in 1 l of Sf9 cell suspension at a cell density of approximately 1×10^6 cells/ml, which was split into two 2l Erlenmeyer flasks. Infection of cells was induced by adding 10 ml of P2 stock virus in each flask. Cells were harvested after 3 days of incubation at 27.5°C (125 rpm).

4.3.3 Cell lysis

The cell culture was centrifuged for 20 min at 5,000 RPM (JLA-9.1000 rotor, *Backman Coulter*) in a centrifuge precooled to 4 °C. The supernatant was discarded and the pellet was resuspended in 100 ml of lysis buffer. Cells were sonicated on ice at 40 % of amplitude using a 10 s On/ 20 s Off cycle for a total time of 7 minutes. The lysate was centrifuged at 40,000×g for 30 min at 4°C. The supernatant was gathered and filtered using a 0.2 μm filter unit.

4.3.4 Ion metal affinity chromatography

In the first purification step, ion metal affinity chromatography was used using a HisTrap FF 5 ml column to bind the full-length qMICAL or the truncated form of qMICAL, which were expressed with the 8×His tag at C-terminus. Prior to purification, the column was thoroughly washed and equilibrated with ultrapure water and the IMAC binding buffer. The filtered cell lysate was then loaded through the pump system running at a 5 ml/min flow rate. Afterwards, the column was washed with 3 column volumes of IMAC binding buffer and then with the IMAC wash buffer until the absorbance reached a steady baseline. After that, the column was washed with ca. 5 column volumes of the IMAC elution buffer and the eluent was collected.

4.3.5 Anion exchange chromatography

The buffer exchange was done by concentrating the protein solution in a 50 kDa MWCO concentrator to approximately 2 ml and diluting it with the AEX loading buffer (15 mM Tris-HCl, 10 mM NaCl, 2mM DTT, pH 8.0) to ≈25 ml and then repeating this step again. The sample was afterwards loaded onto the Q-sepharose column, which was equilibrated in the AEX loading buffer. The flow rate was 5 ml/min and the protein was eluted by the AEX elution buffer (10 mM Tris-HCl, 1 M NaCl, 2 mM DTT, pH 8.0) ranging from 0 - 100 % in 30 minutes gradient.

4.3.6 Concentration and size exclusion chromatography

The concentration of the eluent from AEX was done using a 50 kDa MWCO concentrator, which was previously washed with SEC buffer. The sample was centrifuged in the concentrator at 4,000×g until the volume was reduced to approximately 0.5 ml. The sample was injected onto Superdex 200 Increase 10/300 GL column (Cytiva) at 0.5 ml/min using the 1ml sample loop. The fractions were collected when the absorbance at 280 nm started to grow. SDS-PAGE electrophoresis was used to detect fractions containing the protein of interest and confirm the integrity and purity of the protein. The protein concentration was calculated from its absorbance at 280 nm.

4.3.7 Sodium dodecyl suplhate polyacrylamide gel electrophoresis

For the sodium dodecyl suplhate polyacrylamide gel electrophoresis (SDS-PAGE), 1 - 10 μl of each fraction, depending on the measured concentration, was mixed with 5-14 μl of ultrapure water, and 5 μl of 4× LDS sample buffer to a total volume of 20 μM. Samples were incubated at 95 °C for 5 minutes and centrifuged at 15, 000 × g for 1 minute. 15 μl of each sample was loaded into a NuPAGE 4-12% Bis-Tris gel and the electrophoresis was run at a constant voltage of 200 V for 35 minutes using the MOPS buffer as running buffer.

4.4 Kinetic assay

We used a steady-state kinetic experiment of NADPH oxidation to study the enzymatic properties of *Japanese quail* MICAL-1 and its truncated form (1-979). After purification of both proteins using SEC, the highest purity fractions were chosen according to SDS-PAGE.

4.4.1 F-actin preparation

Rabbit skeletal muscle F-actin (*Cytoskeleton, Inc, 99 % purity*) was prepared according to the manufacturer's data sheet and as described by *Zuchinni et al.* [119]. First, 1 milligram of lyophilized actin was resuspended on ice in 100 μl of ultra-pure water by occasionally pipetting and using the orbital shaker. The actin was dissolved in 5 mM Tris-HCl, pH 8.0, 0.2 $CaCl_2$, 0.2 mM ATP, 5% sucrose, and 1% dextran. The solution was diluted with the G-buffer to a concentration of 0.4 mg/ml and kept on ice for one hour to thoroughly depolymerize any F-actin filaments formed. To remove residual F-actin nucleation centers, actin was transferred to 200 μl ultracentrifuge cuvettes and centrifuged at 100,000 ×g for one hour. After centrifugation, 180 μl of supernatant from each cuvette was transferred to an eppendorf microtube. The concentration of G-actin was measured from the absorbance at 280 nM and the Polymerization buffer was added, in an amount corresponding to 10 % of the entire volume, to induce polymerization. Polymerization was incubated at 25 °C in a water bath for one hour and the F-actin solution was stored on ice. The final buffer (F-buffer) consisted of 9 mM Tris-HCl, pH 8.0, 0.18 mM $CaCl_2$, 1.1 mM ATP, 1.3 mM DTT, 45 mM KCl, and 1.8 mM $MgCl_2$.

4.4.2 NADPH oxidation assay

The rate of NADPH oxidation was measured as a decrease in absorbance in the region of characteristic absorbance for the reduced form of the cofactor. Experiments were conducted in 96-wells UV transparent microtitration plates in triplicate with concentrations of NADPH ranging from 100-4,000 μM for assays without F-actin and 10-500 μM for F-actin assays. NADPH oxidation rates for concentrations ranging from 10-1000 μ M were measured at 340 nm ($\varepsilon_{NADPH,340nm}$ = 6.22 mM l^{-1} cm^{-1}), while higher concentrations (2000-4000) were measured at 374 nm ($\varepsilon_{NADPH,374nm}$ = 2.1 mM l^{-1} cm^{-1}) using the Spark® microplate reader (*Tecan*) at 25 °C.

80 μl of F-buffer or F-actin solution at a concentration of 1.425 μM was pipetted into the microtitration plate and mixed with 20 μl of NADPH solutions dissolved in F-buffer. The reaction was induced by the addition of 20 μl of full-length qMICAL or qMICAL 1-979. The final concentrations of full-length qMICAL and the truncated form were 690 and 110 nM (respectively) for the assay without F-actin, and 100 and 110 nM for the assay with F-actin.

Assays that exhibited linear dependency were analyzed using linear regresion, where the received directive corresponds to the rate of the NADPH oxidation. The values of the directives for each NADPH concentration were plotted and fitted using the Michaelis-Menten equation (Eq. 1, v, reaction rate; v_{max}, maximum reaction rate; $[S]$, substrate concentration; K_m, Michaelis constant) with OriginPro. k_{cat} was calculated using the Eq.2, concentrations of qMICAL forms ($[E]$), were determined from the absorbance at 280 nm.

$$v = \frac{v_{max} \cdot [S]}{K_m + [S]} \tag{1}$$

$$k_{cat} = \frac{v_{max}}{[E]} \tag{2}$$

4.5 Protein crystallization

The purified full-length qMICAL solution (in SEC buffer) was concentrated in a 50 kDa centrifuge concentrator at a concentration of 10 mg/ml and diluted with a solution of 2 mM TCEP at a final concentration of 5 mg/ml (15 mM Tris-HCl, 150 mM NaCl, 2 mM DTT, 1 mM TCEP, pH 8.0). Crystallization trials were conducted by sitting drop-vapor diffusion method with a drop size of 150 nl always using three different protein solution:reservoir solution ratios 2:1, 1:1, and 1:2 and equilibrating against 100 µl of reservoir solution. Crystallization screenings were carried out with JCSG core I, Crystal screen 1 & 2, JCSG+, INDEX, SG1, MPD, INDEX and PACT premier screens. Reservoir solutions were applied to reservoir wells in a 96-well crystallization plate using a Gryphoon dropper (*Art Robbins*) and drops of protein mixture with reservoir solution were applied using the NT8 dropsetter (*Formulatrix*). Crystallization was carried out at 20 °C in the RI1000 crystallization hotel (*Formulatrix*). The experiments were conducted by Dr. Jiří Pavlíček of the Center of Molecular Structure in Biocev.

4.5.1 *In situ* proteolysis crystallization

For in situ proteolysis crystallization, a solution of 1 mg/ml trypsin in acetate buffer was mixed with a solution of qMICAL 3 mg/ml (15 mM Tris-HCl, 50 mM NaCl, 2 mM DTT, 1 mM TCEP) in two different w/w ratios 1:360 and 1:650. The mixture was incubated 1 hour on ice and further used for crystallization screening using Crystal screen 1 & 2, JCSG core I, JCSG+, INDEX, and SG1 screens using the same workflow as described above.

4.6 Multiangle Light Scattering

Oligomeric state of qMICAL in solution was assessed by a multiangle light scattering (MALS) detector (*miniDAWN, Wyatt Technology*) coupled with an Agilent 1200 HPLC system with Biosec-3 SEC column (4.6×300 mm). First, the column was washed with ultrapure water for 1 hour followed by washing with 0.1 M acetic acid for 1 hour and again with ultrapure water for at least 12 hours. Finally, the column was equilibrated in SEC buffer for 3-5hours. All steps were carried out at a flow rate of 0.3 ml / min and stable room temperature.

For each sample, three separate runs were performed with different protein concentrations (2, 1, and 0.5 mg/ml) at a flow rate of 0.3 ml/min. The injection volume was 15 μl. Molecular weight and other parameters were calculated based on protein concentration assessed from absorption at 260 and 280 nm measured by a built-in UV detector (*Agilent Infinity II, Agilent Technologies*), the refractive index determined by the differential refractive index detector (*RI-501 Shodex, Showa Denko*), and MALS data collected at three angles (49°, 90°, 131°) at wavelength 658 nm. The data were analyzed and evaluated with ASTRA software.

4.7 Electron microscopy

For electron microscopy, either freshly purified protein or flash-frozen protein (stored at -80 °C) was used. The latter was thawed prior to use and separated from possible aggregates by size exclusion chromatography. Before application to the EM grid, the samples were centrifuged for 1 minute at 15, 000 ×g.

4.7.1 Negative staining electron microscopy

Negative staining was used to control protein quality and determine the low-resolution structure of the protein. Different concentrations of freshly purified protein solution ranging from 10 to 150 μM were used.

300 mesh 2nm continous carbon Cu EM-grids and glow discharged for 30 seconds prior the sample application. Negative staining was done according to *Booth et al.* [131]. 2 μl of protein solution was applied to the prepared glow discharged grid and after 30 seconds blotted with filtration paper. The grid was afterwards washed in two drops of ultrapure water by touching the drop surface with the grid and then blotting off the residual water. The staining was done by 1 % w/v uranyl formate (first dissolved in boiling ultrapure water and then diluted with 1 M NaOH to prevent precipitation, the final concentration of NaOH was 10 mM). Washed grid was first briefly put on the first drop of the stain and the residual liquid was immediately blotted off by a filter paper (Whatman No. 1). Then it was placed onto the second drop of the stain for 30 seconds, the residual stain was again blotted off, and the grids were left in the fume hood to air-dry. The protein concentration was 15 μg/ml.

Data were collected using software package Serial EM on a JEOL JEM 2100-Plus fitted with a LaB_6 crystal cathode, operating at 200 kV equipped with a TVIPS TemCam–XF416 4K CMOS camera. 423 micrographs were collected at a magnification of 60 000× with a pixel size of 1.905 Å/pixel and a defocus value ranging from 0.5 μm to 2.5 μm.

Collected micrographs were analyzed using Cryosparc software [132]. 332 of the total number of 423 micrographs were selected for further evaluation, based on the CTF fit (contrast transfer function fit), astigmatism, and motion distance parameters. 374,000 particles were picked using an automated Blob picker and filtered through 2D classification with 150 classes. 74,500 particles from the selected 2D classes were used for 3D Ab-initio reconstruction. The 3D protein volume model was fitted with the AlphaFold model of qMCIAL using the UCFS chimera software.

4.7.2 Cryogenic electron microscopy

For cryo-EM analysis, freshly purified qMICAL solution or flash-frozen stored qMICAL repurified by size exclusion chromatography were used. The purified qMICAL was mixed with buffer solutions of detergents (CHAPS, CHAPSO, octyl glucoside) to form solutions at a final protein concentration of 0.25 mg/ml, 0.5 mg/ml, and 1,5 mg/ml. Each sample contained a detergent at a final concentration of 3 mM CHAPS or CHAPSO or 1.8 mM octyl glucoside.

4 μl of the qMICAL solution was applied onto a Cu 1.2/1.3 300 mesh holey carbon EM grid (*Quantifoil*) inside the Leica GP2 plunge freezer chamber with a stable temperature (19 °C) and 90 % humidity. The blotting time was 5 s and the "blot offset" was controlled by the blotting sensor. After being plunged into liquid ethane, the grid was transferred to a cryo-EM grid box and stored in liquid nitrogen until the imaging session.

Data was obtained using the same setup which was used for the negative staining. All micrographs were collected in a low dose mode by Serial EM as a 33 image movie during a total exposure time of 3.62 s (total exposure around 50 $e^-/Å^2$) in a defocus range from 0.5 to 2.5 μm. Micrographs were collected at a magnification of 80,000× with a pixel size of 1.438 Å/pixel.

4.8 Protein structure prediction and molecular dynamics

4.8.1 Structure prediction using Alphafold 2

In the absence of the known structure of MICAL proteins, novel de novo protein structure prediction methods were utilized to determine possible protein folds and to outline the mechanism of MICAL activation. Several different protein prediction runs for qMICAL were performed using Alphafold 2 and Alphafold 2 Multimer [133, 134] (all Alphafold 2 and Alphafold 2 Multimer runs were executed through *https://cosmic2.sdsc.edu/* [135]). First, two models were predicted for the full-length protein and the truncated form of qMCIAL (1-979). Furthermore, full-length qMICAL was modeled as a protein complex treating conserved domains of MICAL proteins (MO, CH, LIM, and C-terminal domains) with known structures as individual protein chains. Linker regions between the domains were excluded from this prediction to assess their impact on domain-domain interactions.

4.8.2 Molecular dynamics using Gromacs

Molecular dynamics simulations of full-length qMICAL and its truncated form (1-979) Alphafold models were performed in Gromacs [136] as described by *Rozbesky et al.* [55]. 10 ns simulations were carried out in triplicate using the AMBER99SB-ILDN force field [137]. First, the protein was immersed in a triclinic box filled with SPC/E water. The minimum distance between the protein and the edge of the box was restricted to 1 nm. The solvent was further treated by adding NaCl to a final concentration of 100 mM using genion. Furthermore, long-range electrostatics were treated with Ewald particle-mesh summation [138] and the P-LINCS algorithm was used to constrain the bond lengths. The simulation pressure (1 atm) and temperature (300 K) were maintained by the Parrinello-Rahman barostat and the v-rescale thermostat, respectively. In the next step, the system energy was minimized using the steepest descent algorithm in 1000 steps. Prior to the simulation, the solvent-solute system was equilibrated for 200 ps with restraint on all non-hydrogen atoms of the protein. The 10 ns simulations were performed with 5 fs integration steps.

Furthermore, an additional 100 ns simulation was performed using the same parameters to investigate whether the 10 ns simulation time is sufficient to explore all possible protein dynamic changes.

5 Results

5.1 Comparison of human and quail MICAL-1 and multiple sequence alignment

MICAL proteins are conserved in all vertebrates. Since no structure for the full protein has yet been published and previous attempts to determine the structure of human MICAL-1 failed, we turned to MICAL-1 from the *Coturnix japonica* (qMICAL, NCBI reference sequence: XP_015740275.1). Avian proteins are, as a result of higher body temperature, more compact and rigid and are often used as model proteins for the structure determination. To evaluate the suitability of qMICAL as a model for human MICAL-1 we performed a pairwise alignment between the protein sequences using the BLOSSOM62 matrix. We also performed an extensive multiple sequence alignment analysis of 286 MICAL-1 sequences from vertebrates, including different protein isoforms for some species. We removed all sequences that did not appear to belong to functional proteins; for example, they lacked one or more motifs necessary for the binding of FAD, missed an entire domain, or another highly conserved region. This narrowed the alignment to 239 sequences.

5.1.1 quail MICAL-1 is a suitable model protein for human MICAL-1

qMICAL is 1131 amino acids long and has 51 % amino acid identity with human hMICAL and 63 % similarity. The most conserved domain is the monooxygenase domain with 69 % identity and 80 % similarity. In addition, all FAD binding motifs, the Rossman fold, GD, and DG motifs, are conserved. Compared to MICAL-2 and MICAL-3, both qMICAL and hMICAL possess a single amino acid alteration in the DG motif (D218A hMICAL, D221G qMICAL) that has been shown to significantly increase protein oxidase activity in the absence of F-actin [107]. Interestingly, this amino acid alteration (D→A/G) is conserved in all vertebrate MICAL-1 proteins, suggesting that it is necessary for their biological function. Furthermore, the tyrosine residue near the C-terminus of the MICAL-1 monooxygenase domain (Y486 qMICAL), which is phosphorylated by Abl kinase and is important for MICAL regulation [121], is also conserved.

The calponin homology domain of qMICAL has 47 % identity and 64 % similarity to the hMICAL CH domain. Both actin and canonical PIP_2 binding sites [102] are preserved, but there is an unconserved region of 16 amino acids that covers the C α-helix and part of the D α-helix of the CH domain in hMICAL, which contains significantly less hydrophobic residues in qMICAL (Fig. 1.6, page 26). This region also exerted a lower conservation rate compared to other species.

The specific motif that forms the LIM domain ($CX_2CX_{17}HX_2CX_2CX_2CX_{19}CX_2H$), which is necessary for the binding of two zinc ions, is precisely preserved in qMICAL and the identity and similarity to the hMICAL LIM domain are 53 % and 60 %, respectively. Interestingly, the C-terminal domain has the second highest conservation score, as it has 61 % identity and 76 % similarity to that of hMICAL. This may be explained by the essential role of the C-terminal domain in the regulation of MICAL-1 activity. In addition, the GTBM motif, for the binding of myosin Va [112], PKPP motif of the proline-rich region, necessary for interaction with the SH3 domain [85], and the newly identified conserved sequence (residues 633-649) in the linker region between the CH and LIM domain, are also preserved.

On the other hand, compared to hMICAL, qMICAL possesses two major amino acid insertions in the linker region between the LIM and C-terminal domains. The first is 28 amino acids long (765-792 of qMICAL and corresponds to 753-754 of hMICAL) and the second is 25 residues long (832-856 of qMICAL and corresponds to 782-783 of hMICAL). Moreover, the Glu-rich region differs in mammals and aves, as covered in the following subsection. In conclusion, qMICAL may serve as a suitable model for human MICAL-1.

5.1.2 Conserved regions and their relevance for MICAL-1 function

Besides MICAL-1 domains, the multiple sequence analysis showed an overall high conservation rate in domains and other regions specific for MICAL-1, such as the GTBM and PPKP motif. Here, we focus on regions where multiple sequence analysis may imply their importance in protein functionality.

Type II calponin homology domains are known to contain the phosphatidylinositol-4,5-bisphosphate (PIP_2) binding site [102]. The PIP_2 binding site, as defined by *Fraley et al.* [139], is a 17 residue-long motif containing at least three basic residues (H/R/K). However, multiple sequence analysis of the MICAL-1 calponin homology domains did not show a conserved motif that could serve as a universal PIP_2 binding site in all MICAL-1 homologues. On the other hand, potential PIP_2 binding sites, following the binding motif derived from PDB structures solved with the PIP_2 molecule ($K/RX_{1-5}K/RX_{8-50}K/R$) [140], are abundant in the CH domains of MICAl-1 proteins. However, they differ significantly in their position in the sequence (Fig. 5.1 A, page 48). For example, residues R517, R520, and R600 of qMICAL form a positively charged surface, which could serve as a PIP_2 binding site; however, of these only arginine at position 517 is conserved in other species.

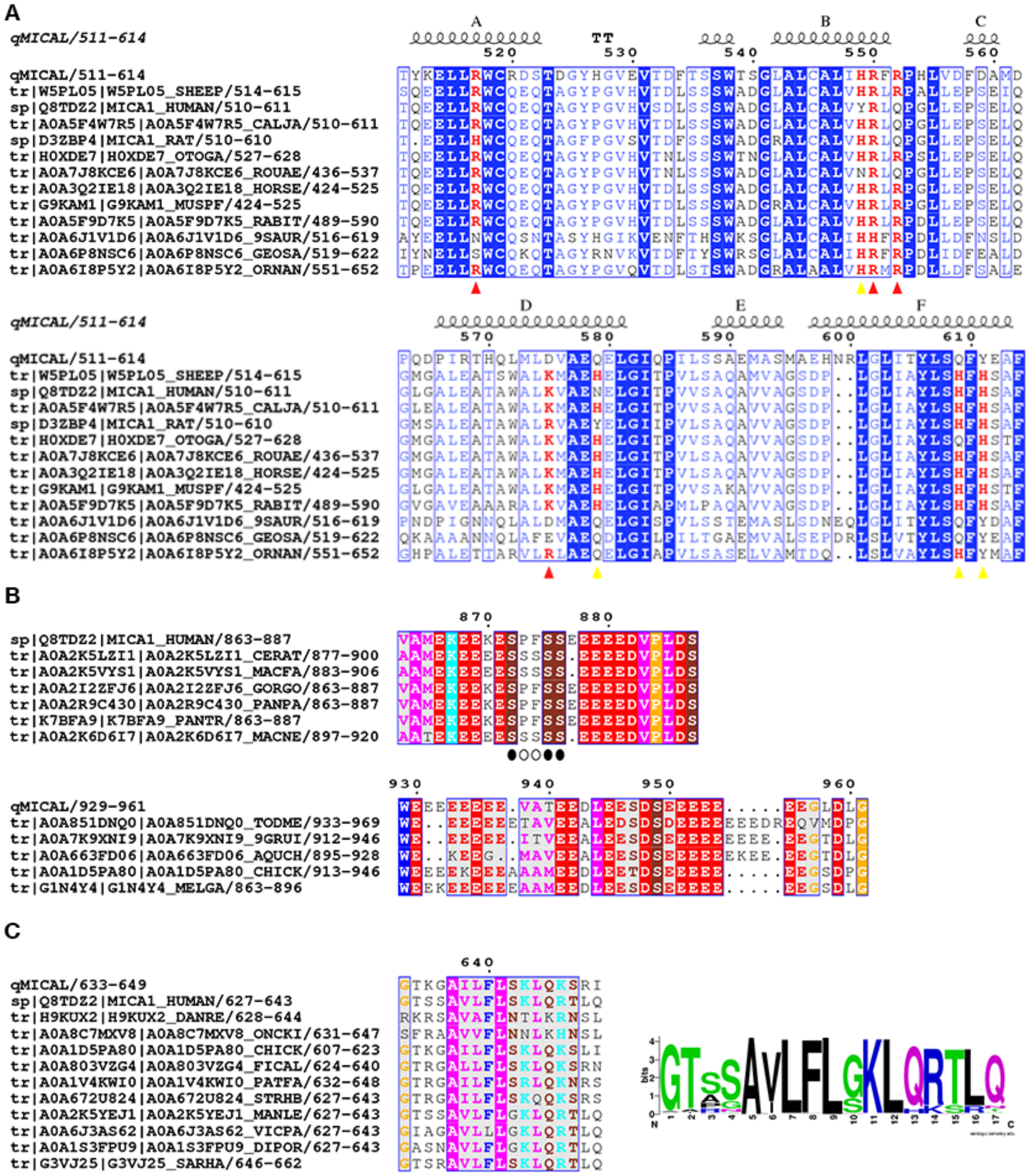

Figure 5.1: ***Multiple sequence alignment of conserved regions from selected species*** *Each sequence represents a group of species with high conservation rate (90 %) A) The calponin homology domains of the MICAL-1 proteins contain the canonical* PIP_2 *binding site (residues 523-538, [102]) but the binding site lacks residues essential for the binding of* PIP_2*. Positively charged residues that facilitate the binding of* PIP_2 *and have conservation greater than 50 % are colored red. The positions where lysine or arginine are conserved are marked with a red triangle, whereas the positions with conserved histidine are marked with a yellow triangle.B) The glutamic acid-rich region differs between the aves and the mammals. The mammalian Glu-rich region is shorter and contains approximately 5 glutamate residues separated by a 5 amino acid serine-rich motif. The avian Glu-rich region is more diverse and lacks the middle conserved part, which is a three-amino acid T/SDS motif.*

Figure 5.1 ***(continued)*****:** *C) multiple sequence alignment of the newly identified conserved sequence (residues 634-649 of qMICAL, left) and the logo representation of the motif (right). The motif is placed in the linker region between the CH and LIM domains. AlphaFold predicts a α-helical secondary structure for the sequence. The most conserved part is the highly hydrophobic 5-amino acid long sequence 636-AV/ILFL-641. The figure was produced with ESPript [141]*

Next, we analyzed the glutamic acid-rich region, which is abundantly mentioned in the literature as a highly conserved region. However, we found that, unlike other conserved regions in MICAL-1 proteins, the Glu-rich region exhibits significant differences between species. For example, the mammalian Glu-rich region is 24-27 amino acids long and contains approximately 10 glutamic residues sequestered by a short sequence rich in serine. On the contrary, in aves, the Glu-rich region extends to around 35 amino acids that contain 14-18 glutamate residues and lacks the serine-rich sequence in the middle (Fig. 5.1 B). The role of the Glu-rich region is still unknown, but differences between classes in the sequence may point to divergent binding affinities.

In addition to known conserved sequences, such as the PKPP motif, necessary for interaction with the SH3 domain, we identified a highly conserved sequence in the linker region between the CH and LIM domains, residues 633-649 of qMICAL (Fig. 5.1 C). This 17 amino acid sequence has not been observed so far and appears to be specific for the MICAL-1 proteins, as we were unable to find similar sequences in other proteins in the protein databases. AlphaFold 2 predicted the α-helical structure for this segment and placed it in the interaction space between the CH, LIM and C-terminal domains so that it contacts all three domains (Fig. 5.2, p. 51).

5.2 Prediction of the qMICAL structure by Alphafold

To obtain a starting structural model of qMICAL we utilized Alphafold for the structure prediction. Alphafold is capable of predicting the structure based on the amino acid sequence of the protein utilizing protein structural databases together with multiple sequence alignment [133].

The predicted structure for full-length qMICAL had high values of pLDDT (70-90 %, predicted Local Distance Difference Test) within the domains (Fig. 5.2 A, B, page 51), which we anticipated because the high-resolution structures of these domains have already been solved [97, 98, 101, 108]. The superposition of the solved structure on the alphafold model showed no significant differences with the values of the root mean square deviation between the structures around 1.5 Å. pLDDT values were much lower in the linker regions, especially in the linker between the LIM and C-terminal domains, where the pLDDT value does not exceed 50 %.

Interestingly, the predicted aligned error (PAE) plot shows relatively high confidence (low values of PAE between residues located in different domains) in positioning of the CH, LIM, and C-terminal domains, which form a partially independent unit (Fig. 5.2 B, C). Furthermore, the region corresponding to the newly identified conserved sequence (residues 634-679) also shows a low PAE value in relation to these domains (Fig. 5.2 B). Although the orientation of the MO domain to other domains appears to be unreliable, its position in the model has interesting implications. The model shows a C-terminal domain bound to the channel leading to the active site of the MO domain. This channel is believed to serve as an access point for the methionine residues of the D-loop of F-actin [97]. Furthermore, the residues responsible for the interdomain contact show a relatively high conservation rate (Fig. 5.2 D).

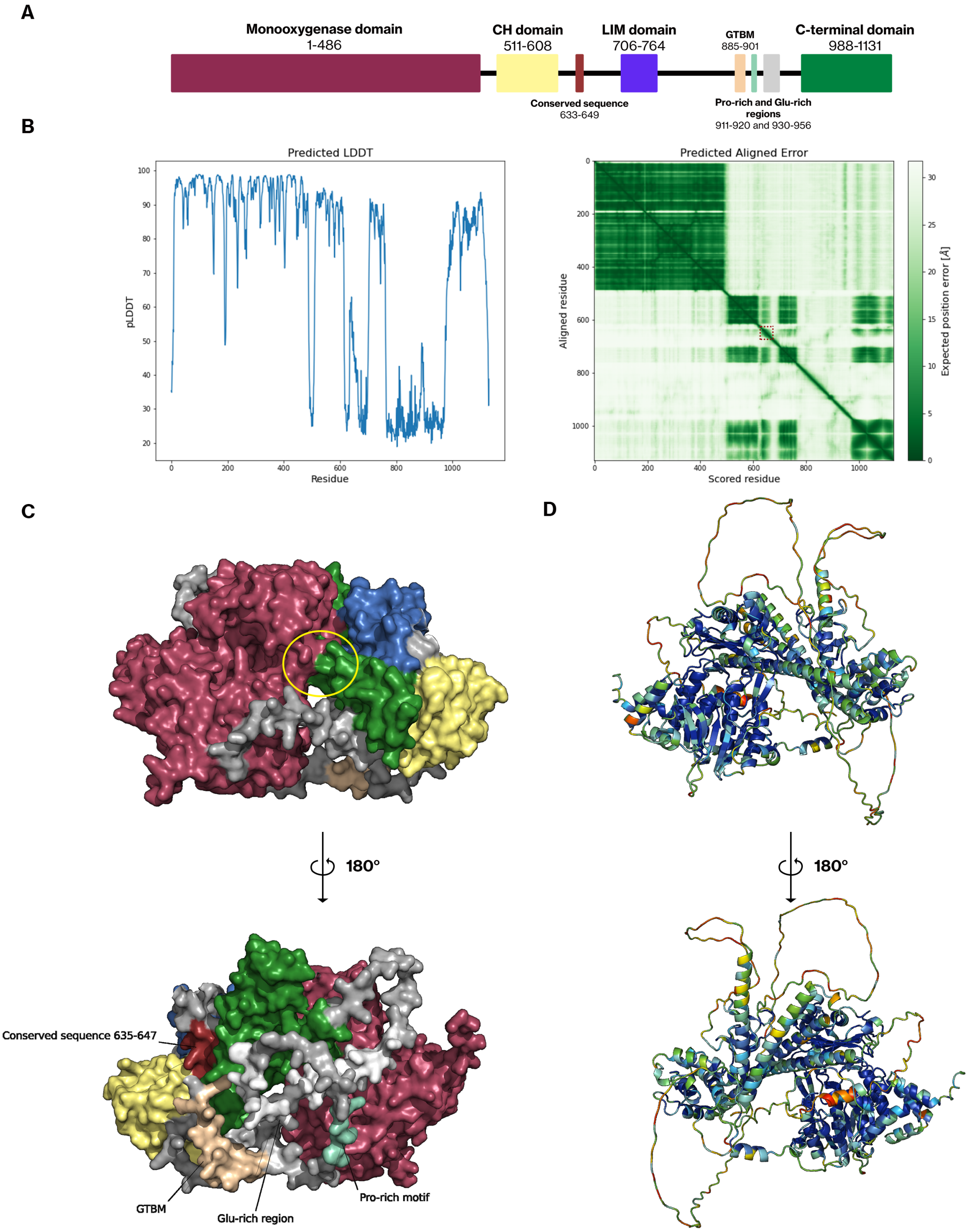

Figure 5.2: ***MICAL-1 domain organization***

A) Scheme of the domain organization of MICAL-1 from Coturnix japonica. B) Plots for the evaluation of the AlphaFold prediction. The plot for the pLDDT (left) shows high structure prediction certainty for the domains of qMICAL but very low pLDDT values for the linker regions. The plot on the right represents the expected position error at residue x (in Å), when the predicted and true structures are aligned on residue y. The green square in the upper left corner of the plot represents the MO domain and then diagonally the CH and LIM, and in the lower right corner the C-terminal domain. AlphaFold is confident in the placement of the CH, LIM, and the C-terminal domains (green rectangles of the diagonal axis), but the predicted error for the positioning of the MO domain and other domains is high. The region corresponding to the newly identified conserved sequence (residues 633-649) is marked with a red dotted square. Note off-diagonal green patches meaning low PAE values for interdomain positioning.

Figure 5.2 ***(continued)*****:** *C) Model of MICAL-1 from Japanese quail in surface representation based on AlphaFold prediction. Domains and conserved regions are colored in corresponding colors to A), and linker regions are colored in gray (linker regions with lowest conservation scores and predicted as disordered (residues 764-883 and 665-703) were removed before visualization for better clarity of domain organization). AlphaFold positioned domains into interesting conformation, where the C-terminal domain, the LIM domain, and the CH domain are forming an almost independent structure interacting with the monooxygenase domain only through the central part of the C-terminal domain. In particular, the C-terminal domain is contacting the MO domain through its N-terminal helix, blocking an access to the active site (yellow circle). The CH and LIM domains are bound to the C-terminal domain on the opposite site. Using multiple sequence alignment, we have identified another conserved region (633-`GTKGAILFLSKLQKSRI`-649) located in the linker between the CH and LIM domains (bottom, colored ruby). AlphaFold predicted the α-helical secondary structure for that sequence. According to the model, this region creates contact with all three domains (C-terminal, LIM, and CH) and may therefore be essential for their interaction (bottom).*

C) Alphafold predicted model of qMICAL in ribbon representation colored by a conservation score from red (lowest conservation score) to blue (highest conservation score). The mostly conserved domain is the monooxygenase domain (top, left side of the model); the dark blue region represents the FAD binding site. Interestingly, the Glu-acid rich region shows lower level of conservation between species (bottom, right; see subsection 5.1, page 46). The figure was produced with PyMol.

5.3 Purification of qMICAL forms

PCR products encoding full-length qMICAL and the truncated form (1-979) were cloned in the pBacPAK9 vector. The truncated form lacking the C-terminal domain was produced to evaluate the impact of the C-terminal domain on the activity and structure of qMICAL. Ligated vectors containing the full-length or truncated form of qMICAL were expressed using the baculoviral expression system. We harvested infected cells and lysed them by sonication, then purified the protein using a combination of affinity, ion exchange, and size-exclusion chromatography. In the final step of purification, proteins were separated by size-exclusion chromatography (Fig. 5.3 A, page 53). Full-length qMICAL was eluted at 11 ml as a well-resolved peak. The first peak in the chromatogram probably corresponds to protein aggregation, as it tended to form when the protein was stored for a longer time.

Interestingly, the chromatogram for the truncated form of qMICAL is much more complex. SDS-PAGE analysis revealed that the protein elutes earlier than the full-length form and corresponds to the second peak of the chromatogram at 10.5 ml. This was confirmed by the NADPH oxidation activity of the protein (see subsection 5.5). Protein purity was evaluated using SDS-PAGE and revealed that both proteins were of relatively good purity (Tab. 2, page 53). Densitometry gel analysis showed that the fractions of purified full-length qMICAL and its truncated form have a purity of approximately 85 % and 81 %, respectively. The total yield from 1 liter of media was approximately 6 mg for the full-length qMICAL and 0.5 mg for the truncated form.

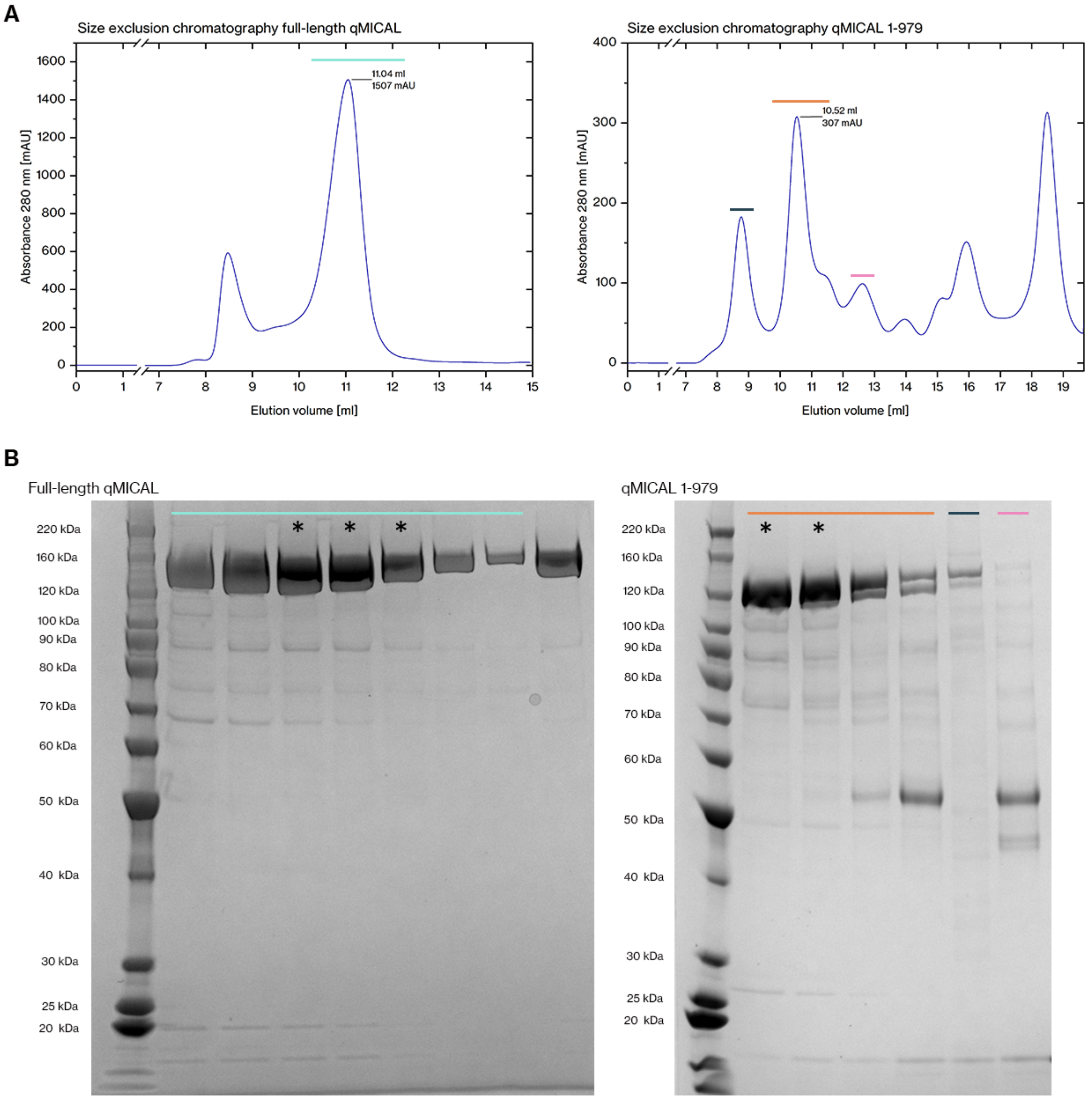

Figure 5.3: ***Purification of the full-length and truncated form of qMICAL***
A) *Elution profiles are from SEC for the full-length (left) and the truncated (right) qMICAL. The full-length protein has an elution volume of 11 ml, whereas the short form of qMICAL elutes at 10.5 ml. This unexpected behavior may be a result of an unstable conformation of the truncated qMICAL, which lacks the C-terminal domain.* ***B)*** *Sodium dodecyl sulfate polyacryl amide gel electrophoresis of purified qMICAL forms. Both proteins elute with minor impurities, but the qMICAL forms were in high surplus to other proteins. Fractions analyzed by SDS-PAGE correspond to SEC peaks marked with the same colored band. Fractions marked with asterisk were used for experiments where high purity of the proteins was needed.*

Table 2: ***Yield and purity of purified full-length qMICAL and qMICAL 1-979***
The purity of proteins was determined using the SDS-PAGE densitometry analysis in ImageJ.

Protein	SEC elution volume (ml)	Mean purity of fractions	Highest purity fraction	Total yield (mg per liter)
full-length qMICAL	11.0	86 ± 5 %	91 %	6
qMICAL 1-979	10.5	81 ± 1 %	82 %	0.5

5.4 Full-lenght qMICAL and its truncated form are monomeric proteins

To investigate whether qMICAL is capable of forming dimers in solution, which can alter its activity, we utilized multiple angle light scattering analysis coupled with size exclusion chromatography. We used three concentrations of the protein ranging from 0.5 mg/ml to 2 mg/ml to examine the oligomeric state in solution at also high concentrations. Full-length qMICAL was eluted at 2.78 ml as a single peak at all three concentrations, without any indications of oligomerization (Fig. 5.4). The calculated molecular weight was 129.1 ± 1.4 kDa, which is in agreement with the theoretical molecular weight of a monomeric protein (129.0 kDa).

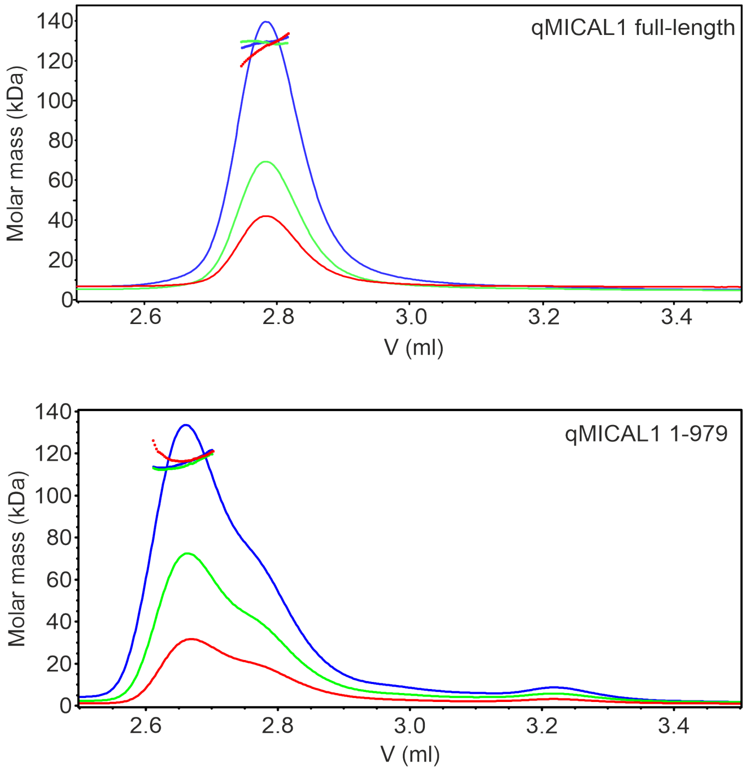

Figure 5.4: ***Size exclusion chromatography coupled with multi angle light scattering analysis***
Full-length qMICAL elutes at 2.78 ml and the truncated form elutes at 2.65 ml. Different curve colors represent different protein concentrations. blue, 2.0 mg/ml ; green, 1.0 mg/ml; red, 0.5 mg/ml

Interestingly, the truncated form had a retention volume of 2.65 ml, suggesting a larger protein than the full-length qMICAL. However, the molecular weight calculated from the multiangle light scattering data showed a molecular weight of 116.4 ± 1.6 kDa, which is about 7 kDa higher than the theoretical molecular weight. The shift in molecular weight may be caused by impurities in the protein solution. On the other hand, the difference in retention volumes between the two forms may imply the structural role of the C-terminal domain, since the truncated form appears to have a larger hydrodynamic radius.

5.5 Kinetics of NADPH oxidation

To better understand the role of the C-terminal domain in protein regulation and the effect of the presence of F-actin on its activity, we performed a series of steady-state kinetic experiments with both the full-length and truncated forms of qMICAL. As MICAL proteins are NADPH dependent, we measured a time-resolved decrease of NADPH specific absorbance (340 nm and 374 nm) that corresponds to the rate of NADPH oxidation catalyzed by the protein. Most importantly, both forms exhibited NADPH oxidase activity, which confirms that they were successfully purified and catalytically active. The experimental setup allowed us to measure the initial rate of the reactions, and therefore analyze the data using the steady-state approximation. All assays showed Michaelis-Menten kinetics as expected (Fig. 5.5, page 56), and we were able to determine the kinetic parameters (Michaelis constant, K_m and catalytic constant, k_{cat}, Tab. 3).

Table 3: ***Steady-state kinetic parameters of NADPH oxidation catalyzed by the full-length and truncated form of qMICAL***
Values of kinetic parameters (K_m, v_{max}) were received by fitting the collected data with the Michaelis-Menten function and used for the calculation of k_{cat} and k_{cat}/K_m. The concentration of qMICAL was measured using the absorbance at 280 nm and the theoretical extinction coefficient, and the concentration of F-actin is expressed as a concentration of G-actin before polymerization. Error propagation was treated using the Gaussian rules of error propagation.

Protein, (nM)	F-actin (nM)	K_m (μM)	k_{cat} (s^{-1})	k_{cat}/K_m ($s^{-1}mM^{-1}$)
qMICAL, 690	-	1461 ± 119	1.14 ± 0.07	0.78 ± 0.07
qMICAL, 100	950	490 ± 96	1.01 ± 0.10	2.07 ± 0.38
qMICAL 1-979, 110	-	1527 ± 76	8.36 ± 0.13	5.47 ± 0.28
qMICAL 1-979, 110	950	1900 ± 1382	7.22 ± 4.34	3.80* ± 3.59

* The kinetic parameters for this reaction were poorly determined, as we expected a much lower K_m value.

Full-length qMICAL exhibited a relatively low affinity for NADPH with a K_m value of approximately 1500 μM and a k_{cat} of 1.15 s^{-1}. These parameters are also well determined, as the relative deviation does not exceed 10 % and are the first reported for a full-length MICAL-1 protein under these conditions (F-buffer, pH 8.0). Interestingly, the addition of F-actin, a substrate of MICAL proteins, led to a significant increase in the affinity for NADPH, but did not change the catalytic constant for the NADPH oxidation by qMICAL (Tab. 3). This could be explained by the conformational changes resulting from the interaction with F-actin. Binding of F-actin may stabilize the "out" conformation of FAD in the MO domain, which has a higher affinity for NADPH than the "in" conformation [142]. However, the catalytic constant remains unchanged as the rate-limiting step, the movement of the FAD to the "in" position, would remain unaffected.

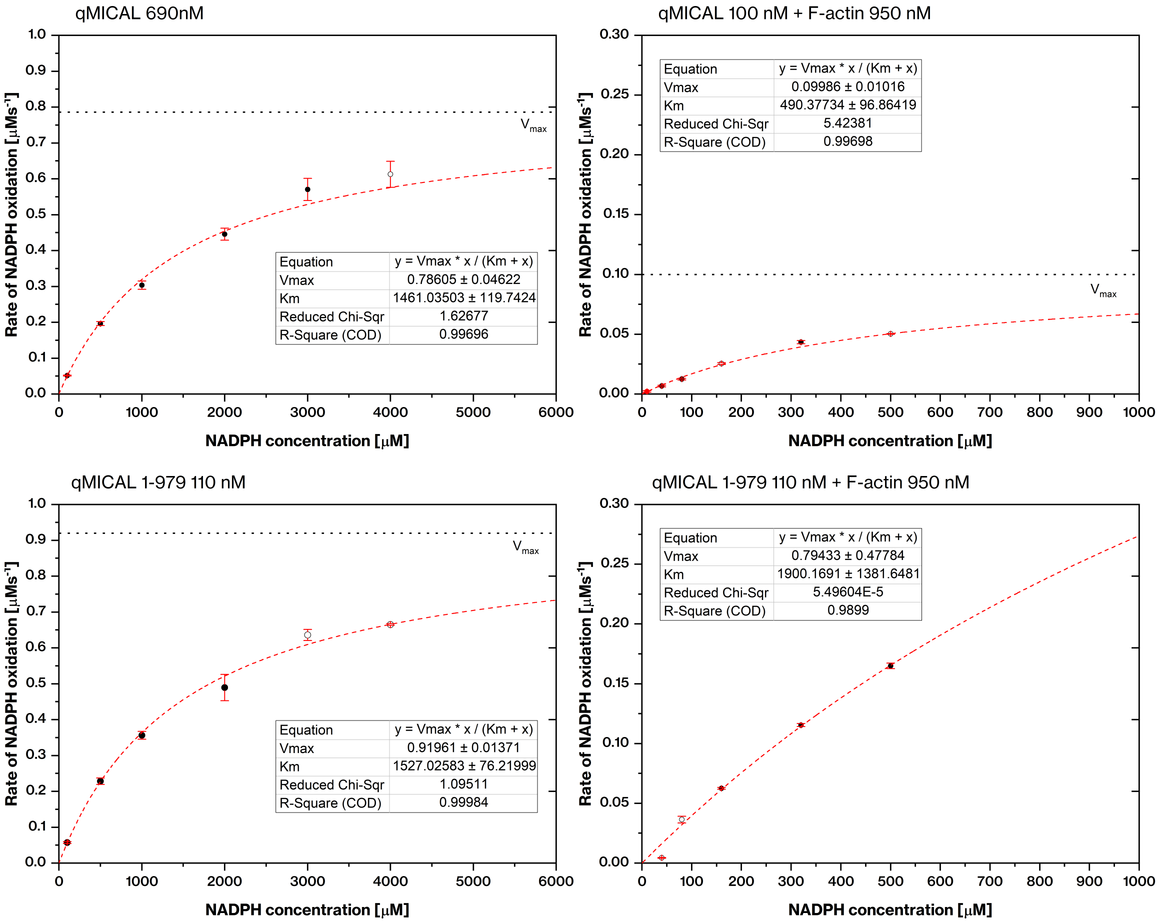

Figure 5.5: ***Steady-state kinetics assay of qMICAL catalyzed oxidation of NADPH in the presence and absence of F-actin***
Rate of NADPH oxidation was measured as the time-resolved decrease in specific absorbance at 340 nm for NADPH concentration 10-1000 µM ($\varepsilon_{NADPH,340nm}$ = *6.22 mM* $l^{-1}cm^{-1}$) *and at 374 nm for NADPH concentrations 2000-4000 µM* ($\varepsilon_{NADPH,374nm}$ = *2.1 mM* $l^{-1}cm^{-1}$)*. Experiments were conducted in technical triplicate (black points), but several outlying data were excluded from the analysis. The points where only two measurements were used for analysis are represented by empty circles. The red point was excluded from fitting with the Michaelis-Menten equation, because of the poor linearity of the rate of NADPH oxidation. Note that graphs in columns are displayed at the same scale.*

Furthermore, removal of the C-terminal domain caused a significant enhancement of the qMICAL catalytic activity, suggesting that it allows for a more rapid transition between the FAD conformations. Interestingly, we did not observe notable differences in the affinities of both forms for NADPH. The analysis also did not reveal any reduction in K_m of the truncated form by adding F-actin, but the parameters of this assay were only poorly determined. However, a direct comparison of steady-state kinetics data in the presence of F-actin between full-length qMICAL and truncated form shows (Fig. 5.5) that the catalytic activity of the truncated form is much higher than the acticity of full-length qMICAL. Although this observation could not be precisely evaluated for K_m from the collected data, it seems that the presence of F-actin has a greater impact on the affinity for NADPH on the full-length protein than on the truncated form lacking the C-terminal domain.

5.6 Molecular dynamics simulations

To elucidate the mechanism of MICAL-1 autoinhibition in the absence of structure, we used a molecular dynamics simulation to explore the possible conformations of qMICAL in solution. First we used AlphaFold 2 to predict the structure of qMICAL for the full-length and truncated form (1-979), which lacks the C-terminal domain.

To investigate whether the structure predicted by Alphafold is relevant and to analyze the overall flexibility of the protein, we performed a 10 ns molecular dynamics simulation of the protein using Gromacs [136]. The subsequent analysis of the movement of the protein backbone showed that qMICAL is relatively rigid in the domain regions, since the values of root mean square fluctuation (RMSF) are below 0.2 nm in most parts of the domains and highly flexible in the linker regions, especially between the LIM and C-terminal domains (Fig. 5.6, page 58). Interestingly, a significant decrease in fluctuation also occurred in other conserved regions, including the Glu-rich region, which in the model interacts with the MO domain. Analysis of the interaction surface using the Adaptive Poisson-Boltzmann Solver (data not shown) revealed that this interaction would be facilitated by strong electrostatic interactions between the negatively charged Glu-rich region and the positively charged surface of the MO domain, formed by K67, K70, K71, H134, R137, K142, K143, and R147. Notably, all those residues are highly conserved across species. Because the Glu-rich region directly precedes the C-terminal domain, it may act as an anchor for the C-terminal domain to keep it in proximity to the MO domain, enhancing their interaction.

A significant decrease in fluctuations was also observed for the conserved sequence (residues 633-349), which is restricted from movement by interactions with the CH, LIM and C-terminal domains. In general, the positioning of the domains remained unchanged throughout the simulation, which is supported by the time evolution of the root mean square deviation (RMSD) of the protein back-bone (Fig. 5.6), which seems to stabilize after several nanoseconds. To confirm this, we performed another 100-ns simulation (data not shown). The RMSD curve reached a plateau after 40 ns, but the most dominant conformational changes occurred in the first 10 nanoseconds of the simulation. Furthermore, the domain organization remained stable throughout the entire simulation time, showing that 10 ns is sufficient time to explore meaningful changes in qMICAL's conformation.

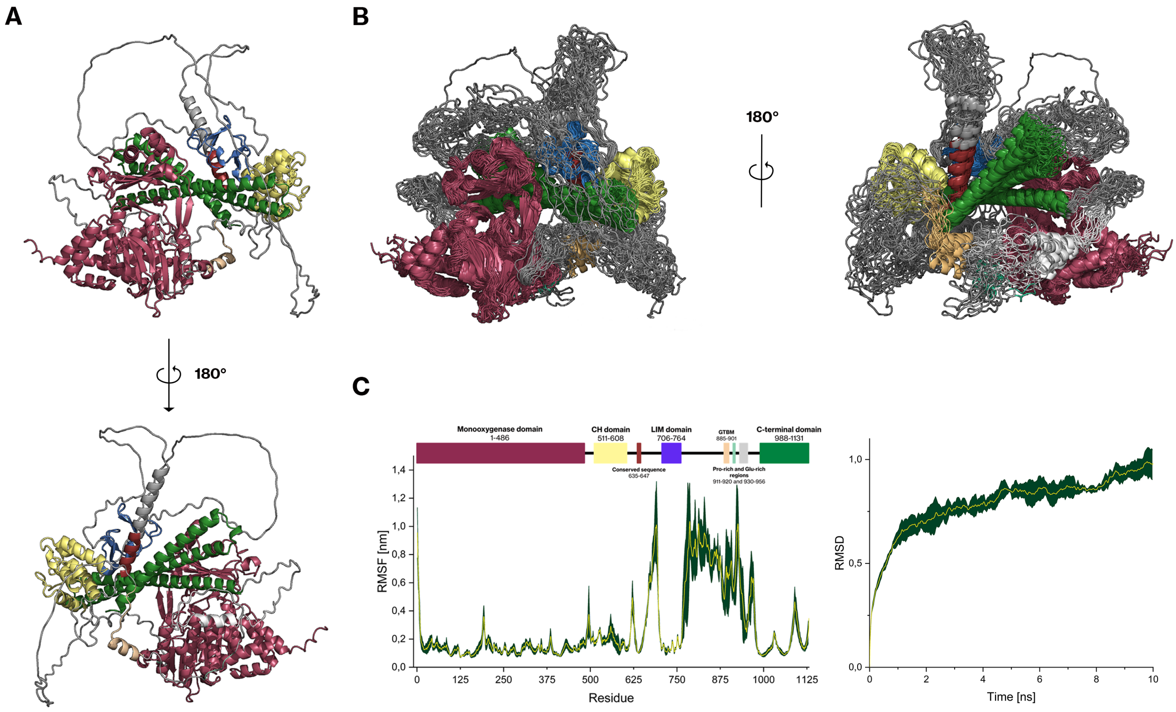

Figure 5.6: ***Predicted structure of qMICAL and molecular dynamics simulation***
Structural model of qMICAL predicted by Alphafold A) and the superposition of 21 qMICAL conformers in cartoon representation extracted every 500 ps of the 10ns simulation B). Note the stability of the domain organization in comparison to unstructured linker regions. Also, the Glu-rich region, which is in contact with the MO domain (right side, white), is relatively stable. C) Analysis of the movement of Cα-atoms of qMICAL during the 10 ns molecular dynamics simulation. Root mean square fluctuations (left) do not exceed 0.3 nm within the qMICAL domains. A significant drop in fluctuations can also be seen in the region corresponding to residues 635-647 of the newly identified conserved sequence and the Glu-rich region. Evolution of the root mean square deviation (right) shows that relatively quickly after the beginning of the simulation the system reaches equilibrium. The structural images were prepared with PyMol.

5.7 Negative staining electron microscopy

To get a low resolution structure of qMICAL and evaluate the suitability of the protein for cryo-EM, we used negative staining microscopy. For negative staining microscopy we used uranyl formate to create a contrast between the protein and the background for electron microscope imaging. Using this method, we were able to collect enough micrographs (Fig. 5.7 A, page 60) to reconstruct the low-resolution model of qMICAL. From nearly 380 000 picked particles, we selected 74 500 particles through the 2D-classification (Fig. 5.7 B). 2D-classification sorts the extracted particles from micrographs into groups, 2D class averages, where each group contains particles with the same orientation. First, we sorted the particles into 100 2D class averages and then selected 28 2D classes representing different orientations of the molecule with the highest number of particles per class. Subsequently, the selected particles were used for 3D ab initio reconstruction in cryosparc. Although the resolution of the resulting model was only 35-40 Å, it was enough to fit the predicted structure into the 3D map (Fig. 5.7 C). The negative staining electron microscopy data show that the structure predicted by AlphaFold may be relevant and represents the autoinhibited conformation of the protein, which would be dominant in the absence of a substrate. However, the resolution and quality of the reconstructed volume are not sufficient to conclude this with certainty.

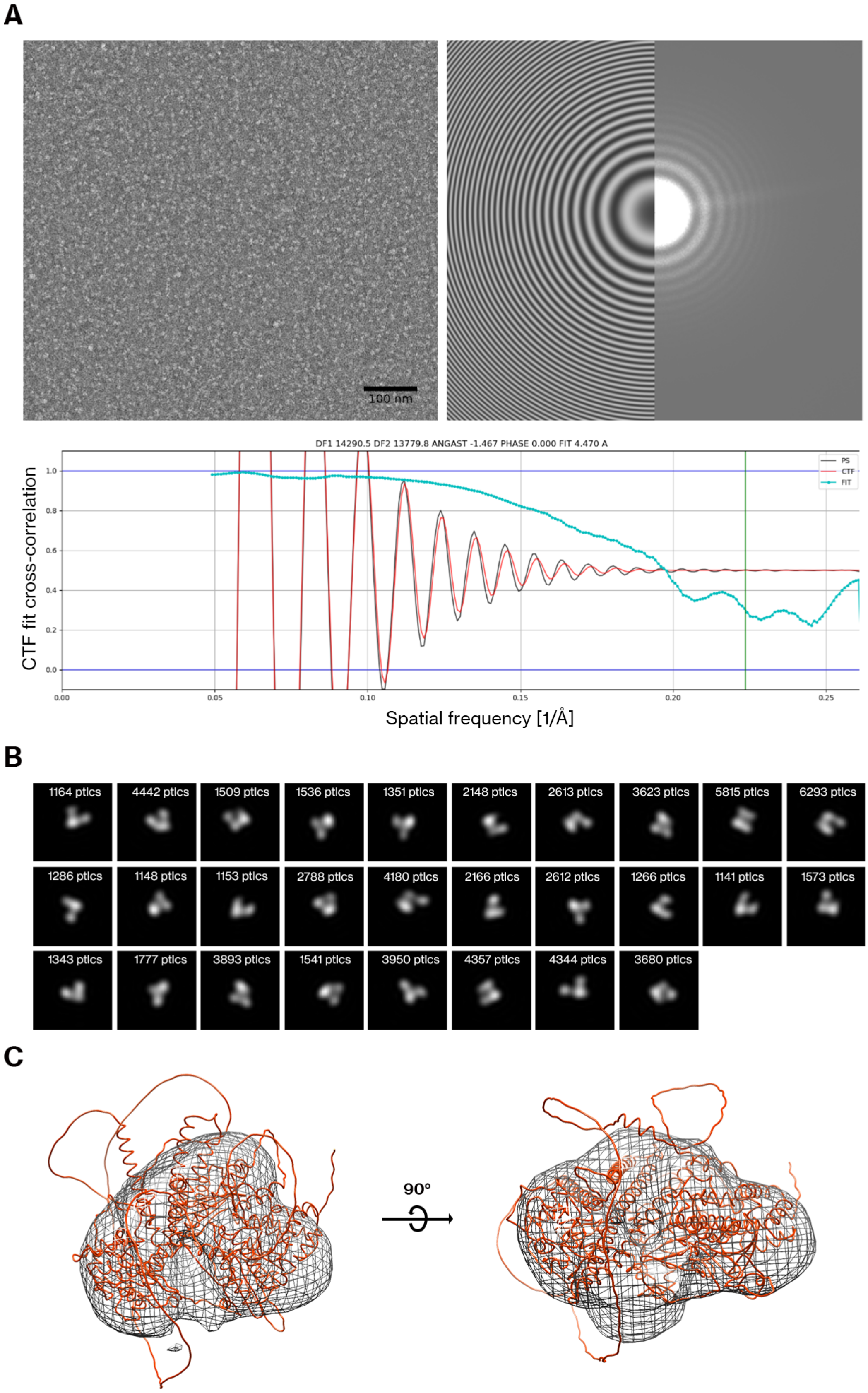

Figure 5.7: *Negative staining electron microscopy workflow*

Figure 5.7 ***(continued)*****:** *A) Example micrograph of negative staining data set (left). Protein particles are white against the uranyl formate stained background. Power spectra of the micrograph and fitted contrast transfer function (right picture, right and left, respectively), and cross-correlation between the power spectra (black curve) and the contrast transfer function fit (red curve) as a function of spatial frequency (A, bottom). The particles were selected using the blob picker and filtered through 2D classification. Selected 2D-classes (B), were used for ab-initio reconstruction of the protein volume. The AlphaFold model of qMICAL was fitted to the volume, which corresponds to the closed conformation of the protein (C). Unstructured linkers and the unconserved regions were excluded from the fitting. The fitting of the structure and the model was performed with the UCSF Chimera modeling system.*

5.8 Cryogenic electron microscopy

After confirmation of protein quality by negative staining electron microscopy, we turned to cryogenic electron microscopy (Cryo-EM). Cryo-EM methods can yield a protein structure (electron density map) with much higher resolution. First, we tried to optimize protein concentration by preparing grids with protein concentrations ranging from 0.5 to 3 mg/ml. To further enhance the consistency of sample preparation, we decided to add a detergent, which should prevent protein aggregation. Therefore, we tested screenings with different dertergent solutions octylglucoside (1.8 mM), CHAPS (3 mM), and CHAPSO (3 mM). As the best condition, we selected CHAPSO at a concentration of 3 mM and a protein concentration of 3 mg/ml. Unfortunately, we were unable to pick enough good quality protein particles for protein structure reconstruction. The sample preparation and screenings were conducted by Dr. Adam Schröfel.

5.9 Crystallization experiments

To assess the high-resolution structure of qMICAL, we performed an extensive crystallization screening. Crystallization experiments were conducted by Dr. Jiří Pavlíček from the Center of Molecular Structure in Biocev. We tried to crystallize the protein using various commercial crystallization screens (see subsection 4.5, page 42). We started with a protein concentration of 8 mg/ml; however, this concentration led to rapid precipitation of the protein. Next, we reduced the concentration to 5 mg/ml, which resulted in a better result, as we observed phase separation or a microcrystalline precipitant in several experiments (Fig. 5.8 A, page 62). Unfortunately, after a year none of the conditions have led to the formation of protein crystals.

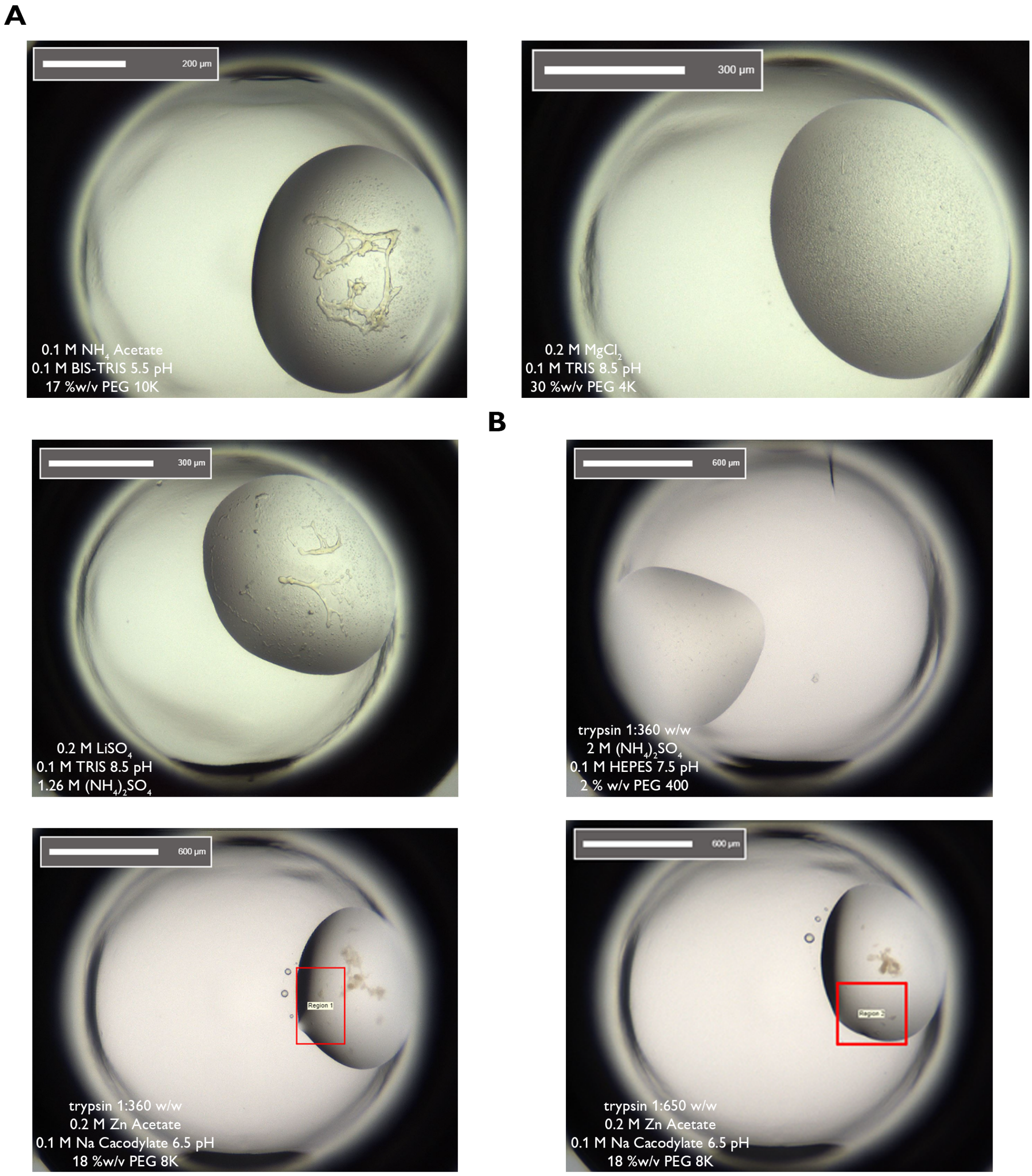

Figure 5.8: ***Sitting drop crystallization experiments***

Crystallization experiments with interesting results for full-length qMICAL A) and in situ proteolysis crystallization of full-length qMICAL B). Experimental conditions are displayed for each drop. Red boxes mark regions where we observed formation of isolated object after two months of crystallization. Protein concentration A) 5 mg/ml; B) 3 mg/ml

With the knowledge of the results of the molecular dynamics simulation, which show that the protein may form a stable conformation in solution, we tried to crystallize the protein without the flexible linker regions. The linker regions were identified as highly flexible disordered peptides and therefore may prevent crystallization. To achieve this, we used the in situ proteolysis crystallization method, using trypsin to cleave exposed parts of the protein and then tried to crystallize the digested protein (Fig. 5.8 B). We selected several promising crystallization conditions from both experiments that could be used as a starting point for optimization.

6 Discussion

The MICAL proteins are a family of flavin monooxygenases that orchestrate the dynamics of the cytoskeleton by mediating F-actin disassembly in various cellular processes in multicellular organisms including axon guidance [84], cytokinesis [109], exocytosis [86] or apoptosis [87]. As these processes are essential for the proper development and function of the organism, it is not surprising that malfunction or unregulated activity of MICAL proteins is linked to many pathological conditions, such as the promotion of breast cancer cell migration through MICAL-2 activity [6] or even neuropsychiatric disorders [91].

MICAL-1 is the only cytosolic protein of the vertebrate MICAL family, lacking the nuclear localization signal. It was discovered to act as a downstream effector of the semaphorin-plexin signaling pathway during axon guidance [84]. Although its function was thought to be primarily to mediate cytoskeleton dynamics through its F-actin monooxygenase activity, recent discoveries show that its field of action may be much broader, as two recently published studies were able to identify novel MICAL-1 substrates. In addition to F-actin, MICAL-1 has been found to oxidize cysteine residues of Peroxiredoxin 1 [123] and Tau protein [143] through its NADPH oxidase activity. This illustrates that MICAL may be involved in many more physiological processes that utilize redox signaling. Elucidating the mechanism of regulation of its monooxygenase and oxidase activity is crucial to understanding its biological role. In this thesis, we utilized various biochemical and biophysical approaches to fully understand the mechanism of MICAL-1 autoinhibition mechanism to open up new pathways for further research.

To understand the mechanism of the MICAL-1 autoregulation, we have focused on the role of the C-teminal domain, which is proposed to attenuate the catalytic activity of MICAL-1 [84, 144]. Although the effect of the C-terminal domain on MICALs activity was studied *in vivo* [84, 109, 144] and *in vitro* [93, 145], no direct interaction of these two domains has been observed yet, as it seems that the C-terminal domain binds rather to a region around the LIM domain than directly to MO domain [84]. One of the proposed mechanisms for the autoinhibition/activation of MICAL-1 is the dimerization of the protein through its C-terminal domain [92]. To address that, we performed a multi-angle light scattering analysis with full-length qMICAL and its truncated form. We show that neither the full-length qMICAL nor the C-terminal domain lacking form oligomerize under standard conditions (subsection 5.4, page 54). These results are in agreement with the observations made by *Esposito et al.*. Using SEC-SAXS (small angle x-ray scattering) analysis of full-length hMICAL in solution, they observed no oligomerization of the protein [93]. An interesting aspect that emerged from our analysis of elution profiles of both forms is that the truncated form elutes earlier than the full-length protein. This can be caused by the loss of a compact structure that would result in a higher hydrodynamic radius of the molecule and therefore a reduction in retention volume as observed (Fig. 5.3, page 53).

MICAL-1 exerts two catalytic activities, produces hydrogen peroxide, and can simultaneously oxidize methionine residues in the D-loop of actin [107]. Both of these processes require NADPH as a cosubstrate and are run through the same catalytic cycle (see Fig. 1.9, page 31, [120]). To study the rate of these reactions, we performed several kinetic assays with both forms of the protein and studied differences in the presence or absence of F-actin. We are the first to report reliable full-length MICAL-1 steady-state kinetic parameters under the conditions used (F-buffer, pH 8.0; see Tab. 3, page 55), which allows us to compare the effect of the presence of F-actin and the removal of the C-terminal domain on the rate of NADPH oxidation. Our results show that F-actin changes the affinity of MICAL-1 for NADPH, lowering the K_m value but not affecting the catalytic constant of NADPH oxidation (Tab. 3, page 55). We hypothesize that this is the result of F-actin-dependent stabilization of the FAD "out" conformation as proposed by *McDonald et al.* in the case of MICAL-2 [142]. The MO domain with FAD in the "out" conformation has a higher affinity to NADPH, which we observed in a steady-state kinetics experiment as a reduction of the K_m value. The catalytic constant remains unchanged because the transition between the "out" and "in" conformations, which is necessary for the oxidative phase of the reaction, is still the rate-limiting step. Similar trends have been reported by *Vitali et al.* in the complex study of human MICAL-1 kinetics [145] with the limitation that they were unable to precisely measure the kinetic parameters for full-length MICAL-1 in the absence of F-actin, which causes difficulties when directly comparing the results.

Interestingly, the absence of the C-terminal domain did not affect the affinity for NADPH, but caused an 8-fold increase in k_{cat}. According to the supposed reaction mechanism, such an increase in the reaction rate can be caused by the faster transition between the "in" and "out" conformations of the protein. If this is the case, the C-terminal domain would have to interact directly or indirectly with the MO domain to slow the conformational changes. We did not observe a dramatic reduction of K_m for the truncated form of qMICAL in the presence of F-actin. However, our results in this case should be interpreted with caution, as we were unable to reliably fit the data, as we expected a much lower K_m value. With these limitations in mind, we can still conclude that the reaction rate was higher than for full-length qMICAL in the presence of F-actin, but the decrease in K_m is less apparent. The latter is opposite to the findings made by *Vitali et al.* as they have determined that $K_{m,F-actin}$ is lower for the truncated form of MICAL-1 than for the full-length protein. These partially contradictory results can be explained by the four times lower concentration of F-actin used in our assays ($\approx 1\ \mu$M compared to $\approx 4\ \mu$M in [145]).

Furthermore, the lower $K_{m,F-actin}$ value does not have to be directly correlated with the increase in the affinity for NADPH induced by F-actin.

Using molecular dynamics simulations, we demonstrate that the AlphaFold prediction of the structure of qMICAL may be of biological relevance. The model provides an interesting insight into a possible MICAL-1 autoinhibition mechanism. In this hypothetical model, the C-terminal domain interacts directly with the MO domain, in particular, in the gap between the monooxygenase and FAD subdomains, close to the opening of the channel that was identified as substrate access and leads directly to the active site [97]. Although no direct interaction between the C-terminal domain and the monooxygenase domain has been reported yet, we assume that this interaction is possible, as the MD simulation showed that this conformation would be stable (Fig. 5.6, page 58). Furthermore, this interaction can be further stabilized by the interaction of the C-terminal domain with the CH and LIM domains and the interaction between the Glu-rich region and the basic surface of the MO domain (see subsection 5.6 and ref. [97]).

According to the predicted model, the CH domain binds to the C-terminal domain at residues 1038-1052, which form the N-terminal part of the middle helix of the coiled coil structure. The linker region connecting the MO and CH domains (residues 487-510) is in this conformation relatively stretched out, which corresponds to the relatively low RMSF values of the protein backbone in this region throughout the simulation (around 0.4 nm, Fig. 5.6, page 58). Therefore, the interaction between the CH and C-terminal domains can serve as a clutch mechanism that stabilizes the closed conformation. The direct interaction between the C-terminal domain and the CH domain in MICAL-1 has been studied *in vitro* by *Rai et al.* and they did not observe any binding [111]. However, they only worked with isolated domains. In another work, the C-terminal domain of MICAL-1 was found to be capable of binding to a construct of the MO, CH, and LIM domains [109]. Furthermore, a similar interaction was successfully studied in the MICAL-like 2 protein (MICAL-L2) by *Sakane et al.* [146]. MICAL-like proteins are closely related to MICAL proteins, consisting of CH and LIM domains pair at the N-terminus, which are connected to the C-terminal domain through a long linker region, similar to MICAL-1. However, MICAL-like proteins lack the monooxygenase domain and therefore do not exhibit catalytic activity. Moreover, MICAL-L2 has the highest similarity to MICAL-1 of MICAL-like proteins, therefore, it may serve as a model protein [147]. *Sakane et al.* provided a comprehensive analysis of the intramolecular interactions of MICAL-L2 and concluded that the C-terminal domain of MICAL-L2 interacts with the CH and LIM domains, when the protein is in the closed inactive conformation [146]. Furthermore, in a subsequent study, they narrowed the identification of the minimum interacting region to the first zinc finger of the LIM domain [148]. However, a pull-down assay with the CH and

LIM domains showed a stronger interaction, suggesting that the LIM and CH domains cooperate in bonding the C-terminal domain [148]. Given these points, we assume that the interplay between the CH and LIM domains can stabilize the closed conformation of the MICAL-1 proteins in a similar way as in MICAL-L2. The question is, how does this closed conformation influence the catalytic activity of MICAL-1?

In the comprehensive analysis of the structure of the murine MICAL-1 MO domain, *Siebold et al.* assume that upon reduction of the FAD molecule, the protein undergoes significant conformational changes that lead to opening of the substrate access channel [97]. In particular, the monooxygenase subdomain must reposition by 6.5° to allow reorganization of amino acid residues blocking the channel [97]. This structural reorganization is specific for the MICAL MO domains in contrast to the structurally related pHBH [56] and is behind the relatively slow transition between the oxidized state (FAD "out") and the reduced state (FAD "in") conformations observed in MICAL proteins [120, 145]. As discussed above, the truncated form of qMICAL exhibits an eight-fold higher catalytic activity; we propose that this is a result of the free movement of the monooxygenase subdomain in the absence of the C-terminal domain. In the closed conformation, the C-terminal domain would work as a wedge between the two subdomains of the MO domain, preventing the repositioning of the monooxygenase domain and therefore reducing the catalytic constant for the whole reaction. To support this hypothesis, we performed another set of MD simulations with the truncated form of qMICAL (data not shown) and, indeed, the region corresponding to the monooxygenase subdomain exerted in the mean approximately 100 % higher RMSF values than during the simulation with full-length qMICAL.

Moreover, our model could also explain the activation of the MICAL-1 protein through interaction with Rab proteins and Plexin receptors. As both proteins were found to interact with the C-terminal domain of MICAL-1 [84, 96, 108]. Their binding could displace the CH and LIM domains, as the predicted binding site for the CH domain partially covers one of the binding sites for Rab proteins [108]. This mechanism was also proposed for the activation of MICAL-L2 by Rab13 [106] and the activation of MICAL-1 by Rab35A [109]. The activation of MICAL-1 activity by the cytoplasmic region of plexin receptors appears to be another candidate for this mechanism, but supporting data have not yet been published.

Interestingly, the MICAL activation mechanism induced by interaction with its substrate, F-actin, appears to follow a different mechanism, as we did not observe an increase in k_{cat} in the presence of F-actin. However, this could be explained by changes in the reaction mechanism when F-actin is present. As described by *Wu et al.* and *McDonald et al.* MICAL proteins can produce hydrogen peroxide simultaneously with the oxidation of actin methionine residues [107, 120]. The last step of the catalytic cycle in which a molecule of water is released from the C4a carbon of flavin hydroxide intermediate (Fig. 1.9) is nearly three times slower than the hydrogen peroxide shunt [120] and could therefore become the rate-limiting step of the reaction. As we only measured the rate of oxidation of NADPH, this would not manifest a change in k_{cat}. However, it remains to be answered whether F-actin binding is sufficient for MICAL-1 activation *in vivo*. For example, overexpression of full-length MICAL-1 in HeLa cells had no effect on actin filaments [144]. The possible explanation for these differences between the *in vivo* and *in vitro* experiments can be provided again by the studies of the MICAL-L2 protein. In their recent work *Sakane et al.* show that different Rab GTPases can affect MICAL-L2 conformation in a opposite way [149]. Rab8A, rather than promoting the opening of the MICAL-L2 structure as Rab13, stabilizes the closed conformation [149]. The analogous influence of some Rab GTPases on MICAL-1 may further dampen its activity in live cells.

In conclusion, we provide a novel model of autoregulation of MICAL catalytic activity through intramolecular interactions between domains (Fig. 6.1, page 69). In this model, the C-terminal domain prevents a rapid transition between the two conformations of the MO domain, which is necessary for the catalytic activity of MICALs and, therefore, slows the reaction rate. We assume that interaction between the MO domain and the C-terminal domain is facilitated by other parts of MICAL-1, in particular the CH and LIM domains and possibly also the Glu-rich region. When MICAL-1 activators, such as Rab or Plexin, are binded, this conformation is released, and the protein exhibits maximum catalytic activity.

The provided model presents a step forward in our understanding of MICAL proteins regulation. However, more detailed studies of intramolecular MICAL interactions and interactions with MICAL regulator proteins will be needed to gather data that would confirm our hypothesis.

To date, all attempts to solve the structure of MICAL-1 have been unsuccessful. Nevertheless, modern structural biology methods, especially cryo-electron microscopy, can give us the structural information necessary to understand the mechanism of dynamical systems such as MICAL-1. Although the identification of new MICAL-1 substrates [123, 143] suggests that the protein can act relatively promiscuously through hydrogen peroxide production, Prx-1, Tau, and F-actin are still the only known MICAL-1 substrates. The search for other potential MICAL-1 substrates will also be an important step in evaluating the role of MICAL proteins in organisms.

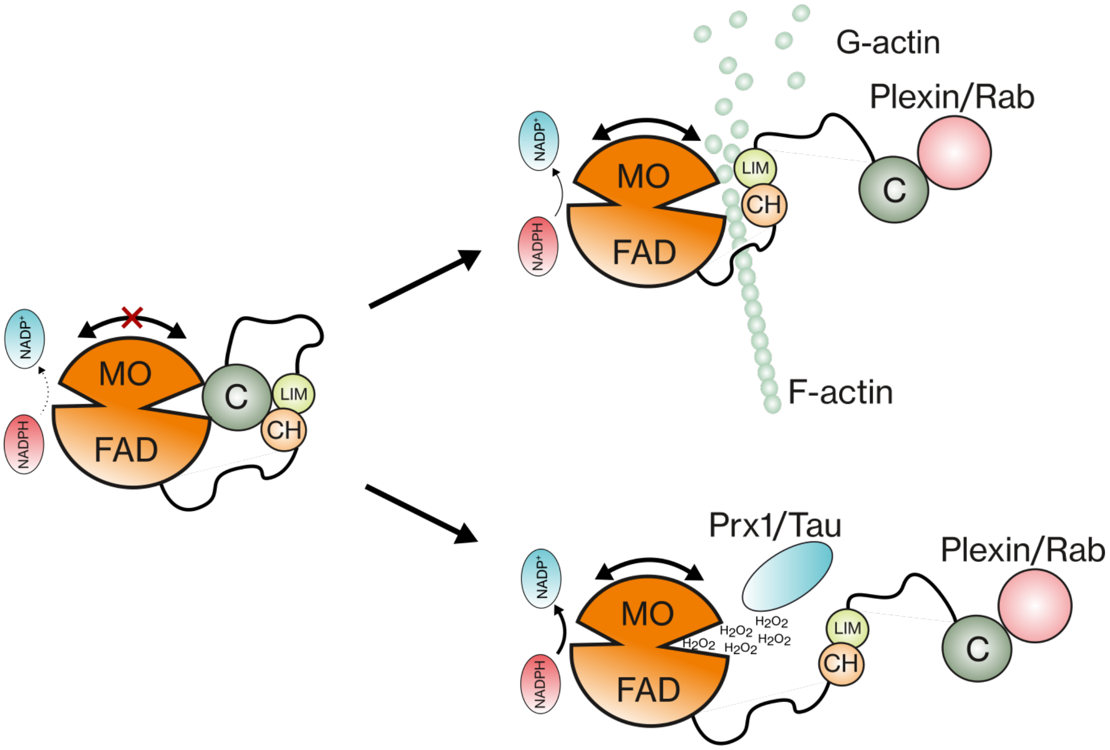

Figure 6.1: ***Scheme of MICAL-1 autoinhibition mechanism and activation***
In the inactive state of MICAL-1, the monooxygenase domain is bound to the C-terminal domain. This binding is strengthened by interaction between the C-terminal domain and the CH and LIM domains. Release from the closed conformation is induced by interaction of the C-terminus with MICAL-1 activators, such as Rab proteins or the cytoplasmic region of plexin receptors. Removal of the C-terminal domain enables a faster transition between the "in" and "out" conformations of the monooxygenase domain (illustrated by curved arrows) and therefore enhances the reaction rate. MICAL catalyzes direct oxidation of methionine residues of F-actin [107] or can act through the production of hydrogen peroxide as in the case of Prx1 [123] and the Tau protein [143]. MO, monooxygenase subdomain; FAD, FAD binding subdomain; CH, calponin homology domain; LIM, LIM domain; C, C-terminal domain

7 Conclusion

- We have successfully produced full-length MICAL-1 from *Coturnix japonica* and its truncated form (residues 1-979) in the Sf9 cell line using the baculoviral expression system and purified both proteins using chromatography methods.
- Using size exclusion chromatography coupled with multiangle light scattering, we have determined that qMICAL and the truncated form of qMICAL (1-979) are monomeric proteins in solution.
- We determined the kinetic parameters of NADPH oxidation catalyzed by full-length qMICAL in the presence and absence of F-actin, as well as the kinetic parameters for the truncated form in the absence of F-actin.
- We utilized protein structure prediction and molecular dynamics simulation to design a MICAL-1 autoinhibition mechanistic model that explains reaction kinetic data and can serve as a launchpad for further research.

References

[1] Marc Tessier-Lavigne and Corey S Goodman. “The molecular biology of axon guidance”. *Science* 274.5290 (1996), pp. 1123–1133.

[2] Jonathan A Raper. “Semaphorins and Their Receptors in Vertebrates and Invertebrates”. *Current Opinion in Neurobiology* 10.1 (2000), pp. 88–94.

[3] Jonathan R. Terman et al. “MICALs, a Family of Conserved Flavoprotein Oxidoreductases, Function in Plexin-Mediated Axonal Repulsion”. *Cell* 109.7 (2002), pp. 887–900.

[4] R.-J. Hung, C. W. Pak, and J. R. Terman. “Direct Redox Regulation of F-Actin Assembly and Disassembly by Mical”. *Science* 334.6063 (2011), pp. 1710–1713.

[5] Emanuela Dazzo et al. “Mutations in MICAL-1cause Autosomal-Dominant Lateral Temporal Epilepsy”. *Annals of Neurology* 83.3 (2018), pp. 483–493.

[6] Y. Wang et al. “MICAL2 Promotes Breast Cancer Cell Migration by Maintaining Epidermal Growth Factor Receptor (EGFR) Stability and EGFR/P38 Signalling Activation”. *Acta Physiologica* 222.2 (2018), e12920.

[7] Wenjie Deng et al. “MICAL1 Facilitates Breast Cancer Cell Proliferation via ROS-Sensitive ERK/Cyclin D Pathway”. *Journal of Cellular and Molecular Medicine* 22.6 (2018), pp. 3108–3118.

[8] Laura Anne Lowery and David Van Vactor. “The Trip of the Tip: Understanding the Growth Cone Machinery”. *Nature Reviews Molecular Cell Biology* 10.5 (5 2009), pp. 332–343.

[9] Erik W Dent and Frank B Gertler. “Cytoskeletal dynamics and transport in growth cone motility and axon guidance”. *Neuron* 40.2 (2003), pp. 209–227.

[10] Andrew W Schaefer, Nurul Kabir, and Paul Forscher. “Filopodia and actin arcs guide the assembly and transport of two populations of microtubules with unique dynamic parameters in neuronal growth cones”. *The Journal of cell biology* 158.1 (2002), pp. 139–152.

[11] Cyrus A Wilson et al. “Myosin II contributes to cell-scale actin network treadmilling through network disassembly”. *Nature* 465.7296 (2010), pp. 373–377.

[12] Thomas D Pollard and Julien Berro. “Mathematical models and simulations of cellular processes based on actin filaments”. *Journal of Biological Chemistry* 284.9 (2009), pp. 5433–5437.

[13] Alexander Babich et al. “F-actin polymerization and retrograde flow drive sustained PLCγ1 signaling during T cell activation”. *Journal of Cell Biology* 197.6 (2012), pp. 775–787.

[14] Thomas D. Pollard and John A. Cooper. “Actin, a Central Player in Cell Shape and Movement”. *Science* 326.5957 (2009), pp. 1208–1212.

[15] Xiao-Feng Zhang et al. “Rho-dependent contractile responses in the neuronal growth cone are independent of classical peripheral retrograde actin flow”. *Neuron* 40.5 (2003), pp. 931–944.

[16] Chihung H Lin et al. “Myosin drives retrograde F-actin flow in neuronal growth cones”. *Neuron* 16.4 (1996), pp. 769–782.

[17] Nelson A Medeiros, Dylan T Burnette, and Paul Forscher. “Myosin II functions in actin-bundle turnover in neuronal growth cones”. *Nature cell biology* 8.3 (2006), pp. 216–226.

[18] Alexander Mogilner and Boris Rubinstein. “The physics of filopodial protrusion”. *Biophysical journal* 89.2 (2005), pp. 782–795.

[19] Jack Bateman and David Van Vactor. “The Trio family of guanine-nucleotide-exchange factors: regulators of axon guidance”. *Journal of cell science* 114.11 (2001), pp. 1973–1980.

[20] Steven M Shamah et al. “EphA receptors regulate growth cone dynamics through the novel guanine nucleotide exchange factor ephexin”. *Cell* 105.2 (2001), pp. 233–244.

[21] Sadig Niftullayev and Nathalie Lamarche-Vane. “Regulators of Rho GTPases in the nervous system: molecular implication in axon guidance and neurological disorders”. *International journal of molecular sciences* 20.6 (2019), p. 1497.

[22] Stephen L Rogers et al. “Drosophila RhoGEF2 associates with microtubule plus ends in an EB1-dependent manner”. *Current Biology* 14.20 (2004), pp. 1827–1833.

[23] Daniel J Goldberg et al. “Recruitment of the Arp2/3 complex and mena for the stimulation of actin polymerization in growth cones by nerve growth factor”. *Journal of neuroscience research* 60.4 (2000), pp. 458–467.

[24] Erin D Goley and Matthew D Welch. “The ARP2/3 complex: an actin nucleator comes of age”. *Nature reviews Molecular cell biology* 7.10 (2006), pp. 713–726.

[25] James E Bear et al. “Antagonism between Ena/VASP proteins and actin filament capping regulates fibroblast motility”. *Cell* 109.4 (2002), pp. 509–521.

[26] Chi W Pak, Kevin C Flynn, and James R Bamburg. “Actin-binding proteins take the reins in growth cones”. *Nature Reviews Neuroscience* 9.2 (2008), pp. 136–147.

[27] Christopher S Cohan et al. “Role of the actin bundling protein fascin in growth cone morphogenesis: localization in filopodia and lamellipodia”. *Cell motility and the cytoskeleton* 48.2 (2001), pp. 109–120.

[28] Josephine Clare Adams and Martin Alexander Schwartz. “Stimulation of fascin spikes by thrombospondin-1 is mediated by the GTPases Rac and Cdc42”. *The Journal of cell biology* 150.4 (2000), pp. 807–822.

[29] Asier Jayo, Maddy Parsons, and Josephine C Adams. “A novel Rho-dependent pathway that drives interaction of fascin-1 with p-Lin-11/Isl-1/Mec-3 kinase (LIMK) 1/2 to promote fascin-1/actin binding and filopodia stability”. *BMC biology* 10.1 (2012), pp. 1–19.

[30] Matilda A Haas, James C Vickers, and Tracey C Dickson. “Rho kinase activates ezrin-radixin-moesin (ERM) proteins and mediates their function in cortical neuron growth, morphology and motility in vitro”. *Journal of neuroscience research* 85.1 (2007), pp. 34–46.

[31] Julian Ng and Liqun Luo. “Rho GTPases regulate axon growth through convergent and divergent signaling pathways”. *Neuron* 44.5 (2004), pp. 779–793.

[32] Kevin C Flynn et al. “ADF/cofilin-mediated actin retrograde flow directs neurite formation in the developing brain”. *Neuron* 76.6 (2012), pp. 1091–1107.

[33] Jeremy Roland et al. “Stochastic severing of actin filaments by actin depolymerizing factor/cofilin controls the emergence of a steady dynamical regime”. *Biophysical journal* 94.6 (2008), pp. 2082–2094.

[34] Omotola F. Omotade, Stephanie L. Pollitt, and James Q. Zheng. “Actin-Based Growth Cone Motility and Guidance”. *Molecular and Cellular Neuroscience.* Cytoskeleton-Dependent Regulation of Neuronal Network Formation 84 (2017), pp. 4–10.

[35] Tito Serafini et al. “The Netrins Define a Family of Axon Outgrowth-Promoting Proteins Homologous to C. Elegans UNC-6”. *Cell* 78.3 (1994), pp. 409–424.

[36] Patrick Mehlen and Laetitia Mazelin. “The Dependence Receptors DCC and UNC5H as a Link between Neuronal Guidance and Survival”. *Biology of the Cell* 95.7 (2003), pp. 425–436.

[37] S. A. Colamarino and M. Tessier-Lavigne. “The Axonal Chemoattractant Netrin-1 Is Also a Chemorepellent for Trochlear Motor Axons”. *Cell* 81.4 (1995), pp. 621–629.

[38] Nicholas P. Boyer and Stephanie L. Gupton. “Revisiting Netrin-1: One Who Guides (Axons)”. *Frontiers in Cellular Neuroscience* 12 (2018), p. 221.

[39] J. J. Brudvig et al. “MARCKS Is Necessary for Netrin-DCC Signaling and Corpus Callosum Formation”. *Molecular Neurobiology* 55.11 (2018), pp. 8388–8402.

[40] Mayya Meriane et al. “Phosphorylation of DCC by Fyn Mediates Netrin-1 Signaling in Growth Cone Guidance”. *The Journal of Cell Biology* 167.4 (2004), pp. 687–698.

[41] Kuan Hong Wang et al. “Biochemical purification of a mammalian slit protein as a positive regulator of sensory axon elongation and branching”. *Cell* 96.6 (1999), pp. 771–784.

[42] Robin Battye, Adrienne Stevens, and J Roger Jacobs. “Axon repulsion from the midline of the Drosophila CNS requires slit function”. *Development* 126.11 (1999), pp. 2475–2481.

[43] Heike Blockus and Alain Chédotal. “Slit-robo signaling”. *Development* 143.17 (2016), pp. 3037–3044.

[44] Hope A Coleman et al. “The Adam family metalloprotease Kuzbanian regulates the cleavage of the roundabout receptor to control axon repulsion at the midline”. *Development* 137.14 (2010), pp. 2417–2426.

[45] Katja Brose et al. “Slit proteins bind Robo receptors and have an evolutionarily conserved role in repulsive axon guidance”. *Cell* 96.6 (1999), pp. 795–806.

[46] Barry J. Dickson. “Molecular Mechanisms of Axon Guidance”. *Science* 298.5600 (2002), pp. 1959–1964.

[47] Erika M. Lisabeth, Giulia Falivelli, and Elena B. Pasquale. “Eph Receptor Signaling and Ephrins”. *Cold Spring Harbor Perspectives in Biology* 5.9 (2013), a009159.

[48] Artur Kania and Rüdiger Klein. “Mechanisms of Ephrin–Eph Signalling in Development, Physiology and Disease”. *Nature Reviews Molecular Cell Biology* 17.4 (4 2016), pp. 240–256.

[49] Elena Seiradake et al. “Structurally encoded intraclass differences in EphA clusters drive distinct cell responses”. *Nature structural & molecular biology* 20.8 (2013), pp. 958–964.

[50] Edgar R Kramer et al. “Cooperation between GDNF/Ret and ephrinA/EphA4 signals for motor-axon pathway selection in the limb”. *Neuron* 50.1 (2006), pp. 35–47.

[51] Laura Taylor Alto and Jonathan R Terman. “Semaphorins and their signaling mechanisms”. *Semaphorin signaling* (2017), pp. 1–25.

[52] Umar Yazdani and Jonathan R. Terman. “The Semaphorins”. *Genome Biology* 7.3 (2006), p. 211.

[53] CS Goodman et al. “Unified nomenclature for the semaphorins/collapsins”. *Cell* 97.5 (1999), pp. 551–552.

[54] A. M. Koppel et al. “A 70 Amino Acid Region within the Semaphorin Domain Activates Specific Cellular Response of Semaphorin Family Members”. *Neuron* 19.3 (1997), pp. 531–537.

[55] Daniel Rozbesky et al. “Diversity of oligomerization in Drosophila semaphorins suggests a mechanism of functional fine-tuning”. *Nature communications* 10.1 (2019), pp. 1–12.

[56] Christian Siebold and E. Yvonne Jones. “Structural Insights into Semaphorins and Their Receptors”. *Seminars in Cell & Developmental Biology*. Semaphorins & Taste Perception 24.3 (2013), pp. 139–145.

[57] David B Kantor et al. “Semaphorin 5A is a bifunctional axon guidance cue regulated by heparan and chondroitin sulfate proteoglycans”. *Neuron* 44.6 (2004), pp. 961–975.

[58] Joris De Wit et al. “Semaphorin 3A displays a punctate distribution on the surface of neuronal cells and interacts with proteoglycans in the extracellular matrix”. *Molecular and Cellular Neuroscience* 29.1 (2005), pp. 40–55.

[59] Bert JC Janssen et al. “Neuropilins lock secreted semaphorins onto plexins in a ternary signaling complex”. *Nature structural & molecular biology* 19.12 (2012), pp. 1293–1299.

[60] Margaret L. Winberg et al. “The Transmembrane Protein Off-Track Associates with Plexins and Functions Downstream of Semaphorin Signaling during Axon Guidance”. *Neuron* 32.1 (2001), pp. 53–62.

[61] Silvia Giordano et al. “The Semaphorin 4D Receptor Controls Invasive Growth by Coupling with Met”. *Nature Cell Biology* 4.9 (9 2002), pp. 720–724.

[62] Jakub M Swiercz, Rohini Kuner, and Stefan Offermanns. “Plexin-B1/RhoGEF–mediated RhoA activation involves the receptor tyrosine kinase ErbB-2”. *The Journal of cell biology* 165.6 (2004), pp. 869–880.

[63] J Falk et al. “G. Rougon, M. Grumet, AW Puschel, JR Sanes, and V. Castellani. 2005. Dual 12 functional activity of semaphorin 3B is required for positioning the anterior 13 commissure”. *Neuron* 48 (0011), pp. 63–75.

[64] V. Castellani et al. “Analysis of the L1-Deficient Mouse Phenotype Reveals Cross-Talk between Sema3A and L1 Signaling Pathways in Axonal Guidance”. *Neuron* 27.2 (2000), pp. 237–249.

[65] Youxin Kong et al. “Structural Basis for Plexin Activation and Regulation”. *Neuron* 91.3 (2016), pp. 548–560.

[66] Zhuhao Wu et al. “A combinatorial semaphorin code instructs the initial steps of sensory circuit assembly in the Drosophila CNS”. *Neuron* 70.2 (2011), pp. 281–298.

[67] Jonathan R Terman and Alex L Kolodkin. “Nervy links protein kinase a to plexin-mediated semaphorin repulsion”. *Science* 303.5661 (2004), pp. 1204–1207.

[68] Yeping Zhou, Rou-Afza F. Gunput, and R. Jeroen Pasterkamp. “Semaphorin Signaling: Progress Made and Promises Ahead”. *Trends in Biochemical Sciences* 33.4 (2008), pp. 161–170.

[69] Sophie Chauvet et al. “Gating of Sema3E/PlexinD1 signaling by neuropilin-1 switches axonal repulsion to attraction during brain development”. *Neuron* 56.5 (2007), pp. 807–822.

[70] Toshihiko Toyofuku et al. “FARP2 triggers signals for Sema3A-mediated axonal repulsion”. *Nature neuroscience* 8.12 (2005), pp. 1712–1719.

[71] Yuxiao Wang et al. “Plexins are GTPase-activating proteins for Rap and are activated by induced dimerization”. *Science signaling* 5.207 (2012), ra6–ra6.

[72] Yuxiao Wang et al. “Structural basis for activation and non-canonical catalysis of the Rap GTPase activating protein domain of plexin”. *Elife* 2 (2013), e01279.

[73] Tomoyo Okada et al. “The Rho GTPase Rnd1 suppresses mammary tumorigenesis and EMT by restraining Ras-MAPK signalling”. *Nature cell biology* 17.1 (2015), pp. 81–94.

[74] Silvio M Zanata et al. “Antagonistic effects of Rnd1 and RhoD GTPases regulate receptor activity in Semaphorin 3A-induced cytoskeletal collapse”. *Journal of Neuroscience* 22.2 (2002), pp. 471–477.

[75] Yufeng Tong et al. “Binding of Rac1, Rnd1, and RhoD to a novel Rho GTPase interaction motif destabilizes dimerization of the plexin-B1 effector domain”. *Journal of Biological Chemistry* 282.51 (2007), pp. 37215–37224.

[76] Huawei He et al. “Crystal structure of the plexin A3 intracellular region reveals an autoinhibited conformation through active site sequestration”. *Proceedings of the National Academy of Sciences* 106.37 (2009), pp. 15610–15615.

[77] Yanyan Liu et al. “A putative structural mechanism underlying the antithetic effect of homologous RND1 and RhoD GTPases in mammalian plexin regulation”. *Elife* 10 (2021), e64304.

[78] Yuri Ito et al. “Sema4D/plexin-B1 activates GSK-3β through R-Ras GAP activity, inducing growth cone collapse”. *EMBO reports* 7.7 (2006), pp. 704–709.

[79] Yuko Fukata et al. “CRMP-2 binds to tubulin heterodimers to promote microtubule assembly”. *Nature cell biology* 4.8 (2002), pp. 583–591.

[80] Thomas Leung et al. “A novel serine/threonine kinase binding the Ras-related RhoA GTPase which translocates the kinase to peripheral membranes”. *Journal of Biological Chemistry* 270.49 (1995), pp. 29051–29054.

[81] Bart C Jongbloets and R Jeroen Pasterkamp. “Semaphorin Signalling during Development”. *Development (Cambridge, England)* 141.17 (2014), pp. 3292–3297.

[82] Joseph C Ayoob, Jonathan R Terman, and Alex L Kolodkin. “Drosophila Plexin B is a Sema-2a receptor required for axon guidance” (2006).

[83] Ruei-Jiun Hung. “Mical Links Semaphorins to F-Actin Disassembly”. 463 (2010), p. 5.

[84] Eric F. Schmidt, Sang-Ohk Shim, and Stephen M. Strittmatter. “Release of MICAL Autoinhibition by Semaphorin-Plexin Signaling Promotes Interaction with Collapsin Response Mediator Protein”. *Journal of Neuroscience* 28.9 (2008), pp. 2287–2297.

[85] Takahiro Suzuki et al. “MICAL, a Novel CasL Interacting Molecule, Associates with Vimentin”. *Journal of Biological Chemistry* 277.17 (2002), pp. 14933–14941.

[86] Yeping Zhou et al. “MICALs in Control of the Cytoskeleton, Exocytosis, and Cell Death”. *Cellular and Molecular Life Sciences* 68.24 (2011), pp. 4033–4044.

[87] Yeping Zhou et al. “MICAL-1 Is a Negative Regulator of MST-NDR Kinase Signaling and Apoptosis▿”. *Molecular and Cellular Biology* 31.17 (2011), pp. 3603–3615.

[88] Jimok Yoon and Jonathan R. Terman. “MICAL Redox Enzymes and Actin Remodeling: New Links to Classical Tumorigenic and Cancer Pathways”. *Molecular & Cellular Oncology* 5.1 (2018), e1384881.

[89] Thorsten Müller et al. “Modulation of Gene Expression and Cytoskeletal Dynamics by the Amyloid Precursor Protein Intracellular Domain (AICD)”. *Molecular Biology of the Cell* 18.1 (2007), pp. 201–210.

[90] Juana M Pasquini, Laura A Pasquini, and Hector R Quintá. “Oxidative Stress and Neurodegeneration”. In: *Biochemistry of Oxidative Stress.* Springer, 2016, pp. 309–325.

[91] Peng Jiang et al. “A Systems Approach Identifies Networks and Genes Linking Sleep and Stress: Implications for Neuropsychiatric Disorders”. *Cell Reports* 11.5 (2015), pp. 835–848.

[92] Maria Antonietta Vanoni. “Structure-Function Studies of MICAL, the Unusual Multidomain Flavoenzyme Involved in Actin Cytoskeleton Dynamics”. *Archives of Biochemistry and Biophysics* 632 (2017), pp. 118–141.

[93] Alessandro Esposito et al. “Human MICAL1: Activation by the Small GTPase Rab8 and Small-angle X-ray Scattering Studies on the Oligomerization State of MICAL1 and Its Complex with Rab8”. *Protein Science : A Publication of the Protein Society* 28.1 (2019), pp. 150–166.

[94] Mark R. Lundquist et al. “Redox Modification of Nuclear Actin by MICAL-2 Regulates SRF Signaling”. *Cell* 156.3 (2014), pp. 563–576.

[95] Thomas Weide et al. “MICAL-1 Isoforms, Novel Rab1 Interacting Proteins”. *Biochemical and Biophysical Research Communications* 306.1 (2003), pp. 79–86.

[96] Julia Fischer, Thomas Weide, and Angelika Barnekow. “The MICAL Proteins and Rab1: A Possible Link to the Cytoskeleton?” *Biochemical and Biophysical Research Communications* 328.2 (2005), pp. 415–423.

[97] C. Siebold et al. “High-Resolution Structure of the Catalytic Region of MICAL (Molecule Interacting with CasL), a Multidomain Flavoenzyme-Signaling Molecule”. *Proceedings of the National Academy of Sciences* 102.46 (2005), pp. 16836–16841.

[98] Mythili Nadella et al. “Structure and Activity of the Axon Guidance Protein MICAL”. *Proceedings of the National Academy of Sciences* 102.46 (2005), pp. 16830–16835.

[99] Michel HM Eppink, Willem JH Van Berkel, and Herman A Schreuder. “Identification of a novel conserved sequence motif in flavoprotein hydroxylases with a putative dual function in FAD/NAD (P) H binding”. *Protein Science* 6.11 (1997), pp. 2454–2458.

[100] Sonia Bañuelos, Matti Saraste, and Kristina Djinović Carugo. “Structural comparisons of calponin homology domains: implications for actin binding”. *Structure* 6.11 (1998), pp. 1419–1431.

[101] Hongbin Sun et al. “Solution Structure of Calponin Homology Domain of Human MICAL-1”. *Journal of Biomolecular NMR* 36.4 (2006), pp. 295–300.

[102] Mario Gimona et al. “Functional plasticity of CH domains”. *FEBS letters* 513.1 (2002), pp. 98–106.

[103] Saif S Alqassim et al. “Modulation of MICAL monooxygenase activity by its calponin homology domain: structural and mechanistic insights”. *Scientific reports* 6.1 (2016), pp. 1–17.

[104] Xianju Jin et al. “Investigation of the Four Cooperative Unfolding Units Existing in the MICAL-1 CH Domain”. *Biophysical Chemistry* 129.2 (2007), pp. 269–278.

[105] Julie L. Kadrmas and Mary C. Beckerle. “The LIM Domain: From the Cytoskeleton to the Nucleus”. *Nature Reviews Molecular Cell Biology* 5.11 (11 2004), pp. 920–931.

[106] Ayuko Sakane, Kazufumi Honda, and Takuya Sasaki. “Rab13 regulates neurite outgrowth in PC12 cells through its effector protein, JRAB/MICAL-L2”. *Molecular and cellular biology* 30.4 (2010), pp. 1077–1087.

[107] Heng Wu et al. “The MICALs are a family of F-actin dismantling oxidoreductases conserved from Drosophila to humans”. *Scientific reports* 8.1 (2018), pp. 1–20.

[108] Amrita Rai et al. “BMERB Domains Are Bivalent Rab8 Family Effectors Evolved by Gene Duplication”. *eLife* 5 (2018), e18675.

[109] Stéphane Frémont et al. “Oxidation of F-actin controls the terminal steps of cytokinesis”. *Nature communications* 8.1 (2017), pp. 1–16.

[110] Ilya Grigoriev et al. “Rab6, Rab8, and MICAL3 Cooperate in Controlling Docking and Fusion of Exocytotic Carriers”. *Current Biology* 21.11 (2011), pp. 967–974.

[111] Amrita Rai et al. “The mechanism of activation of the actin binding protein EHBP1 by Rab8 family members”. *Nature communications* 11.1 (2020), pp. 1–16.

[112] Fengfeng Niu et al. “F-actin disassembly factor MICAL1 binding to Myosin Va mediates cargo unloading during cytokinesis”. *Science advances* 6.45 (2020), eabb1307.

[113] Elena E Grintsevich et al. “Catastrophic disassembly of actin filaments via Mical-mediated oxidation”. *Nature communications* 8.1 (2017), pp. 1–10.

[114] Nigel G Laing et al. “Mutations and polymorphisms of the skeletal muscle α-actin gene (ACTA1)”. *Human mutation* 30.9 (2009), pp. 1267–1277.

[115] Elena E Grintsevich et al. “F-actin dismantling through a redox-driven synergy between Mical and cofilin”. *Nature cell biology* 18.8 (2016), pp. 876–885.

[116] Elena E. Grintsevich et al. “Profilin and Mical Combine to Impair F-Actin Assembly and Promote Disassembly and Remodeling”. *Nature Communications* 12.1 (1 2021), p. 5542.

[117] Byung Cheon Lee et al. “MsrB1 and MICALs regulate actin assembly and macrophage function via reversible stereoselective methionine oxidation”. *Molecular cell* 51.3 (2013), pp. 397–404.

[118] Bruno Manta and Vadim N. Gladyshev. “Regulated Methionine Oxidation by Monooxygenases”. *Free radical biology & medicine* 109 (2017), pp. 141–155.

[119] Daniela Zucchini et al. “Kinetic and Spectroscopic Characterization of the Putative Monooxygenase Domain of Human MICAL-1”. *Archives of Biochemistry and Biophysics* 515.1 (2011), pp. 1–13.

[120] Claudia Alejandra McDonald. “The Enzymology of the Monooxygenase Domain of MICAL-2.” PhD thesis. 2013.

[121] Jimok Yoon et al. “Amplification of F-actin disassembly and cellular repulsion by growth factor signaling”. *Developmental cell* 42.2 (2017), pp. 117–129.

[122] Shannon K Rich, Raju Baskar, and Jonathan R Terman. “Propagation of F-actin disassembly via Myosin15-Mical interactions”. *Science Advances* 7.20 (2021), eabg0147.

[123] Clara Ortegón Salas et al. “NADPH-dependent oxidation of CRMP2 through a MICAL1-Prx1 redox relay controls neurite outgrowth” (2021).

[124] Alex H Hutagalung and Peter J Novick. “Role of Rab GTPases in membrane traffic and cell physiology”. *Physiological reviews* 91.1 (2011), pp. 119–149.

[125] Mitsunori Fukuda et al. “Large scale screening for novel rab effectors reveals unexpected broad Rab binding specificity”. *Molecular & Cellular Proteomics* 7.6 (2008), pp. 1031–1042.

[126] Akifumi Morinaka et al. “Thioredoxin mediates oxidation-dependent phosphorylation of CRMP2 and growth cone collapse”. *Science signaling* 4.170 (2011), ra26–ra26.

[127] Rahul C Deo et al. “Structural bases for CRMP function in plexin-dependent semaphorin3A signaling”. *The EMBO journal* 23.1 (2004), pp. 9–22.

[128] Fábio Madeira et al. “The EMBL-EBI search and sequence analysis tools APIs in 2019”. *Nucleic acids research* 47.W1 (2019), W636–W641.

[129] Haim Ashkenazy et al. “ConSurf 2010: calculating evolutionary conservation in sequence and structure of proteins and nucleic acids”. *Nucleic acids research* 38.suppl_2 (2010), W529–W533.

[130] Alexandrine Froger and James E Hall. “Transformation of plasmid DNA into E. coli using the heat shock method”. *JoVE (Journal of Visualized Experiments)* 6 (2007), e253.

[131] David S Booth, Agustin Avila-Sakar, and Yifan Cheng. “Visualizing proteins and macromolecular complexes by negative stain EM: from grid preparation to image acquisition”. *JoVE (Journal of Visualized Experiments)* 58 (2011), e3227.

[132] Ali Punjani et al. “cryoSPARC: algorithms for rapid unsupervised cryo-EM structure determination”. *Nature methods* 14.3 (2017), pp. 290–296.

[133] John Jumper et al. “Highly Accurate Protein Structure Prediction with AlphaFold”. *Nature* 596.7873 (7873 2021), pp. 583–589.

[134] Richard Evans et al. “Protein complex prediction with AlphaFold-Multimer”. *BioRxiv* (2021).

[135] MA Cianfrocco et al. “COSMIC2: A science gateway for cryo-electron microscopy structure determination”. In: *Proceedings of the Practice and Experience in Advanced Research Computing 2017 on Sustainability, Success and Impact.* 2017, pp. 1–5.

[136] Mark James Abraham et al. “GROMACS: High performance molecular simulations through multi-level parallelism from laptops to supercomputers”. *SoftwareX* 1 (2015), pp. 19–25.

[137] K Lindorff-Larsen et al. “Improved Side-Chain Torsion Potentials for the Amber Ff99SB Protein Force Field (2010) Proteins: Struct”. *Funct. Bioinforma. NA-NA* ().

[138] Ulrich Essmann et al. “A smooth particle mesh Ewald method”. *The Journal of chemical physics* 103.19 (1995), pp. 8577–8593.

[139] Tamara S Fraley et al. “Phosphoinositide binding inhibits α-actinin bundling activity”. *Journal of Biological Chemistry* 278.26 (2003), pp. 24039–24045.

[140] Giacomo Franzot et al. “The crystal structure of the actin binding domain from α-actinin in its closed conformation: structural insight into phospholipid regulation of α-actinin”. *Journal of molecular biology* 348.1 (2005), pp. 151–165.

[141] Xavier Robert and Patrice Gouet. “Deciphering key features in protein structures with the new ENDscript server”. *Nucleic acids research* 42.W1 (2014), W320–W324.

[142] Claudia A McDonald, Ying Yi Liu, and Bruce A Palfey. “Actin stimulates reduction of the MICAL-2 monooxygenase domain”. *Biochemistry* 52.35 (2013), pp. 6076–6084.

[143] Engie Prifti et al. “Mical modulates Tau toxicity via cysteine oxidation in vivo”. *Acta neuropathologica communications* 10.1 (2022), pp. 1–19.

[144] Sai Srinivas Panapakkam Giridharan et al. “Differential Regulation of Actin Microfilaments by Human MICAL Proteins”. *Journal of Cell Science* 125.3 (2012), pp. 614–624.

[145] Teresa Vitali et al. “Properties and Catalytic Activities of MICAL1, the Flavoenzyme Involved in Cytoskeleton Dynamics, and Modulation by Its CH, LIM and C-Terminal Domains”. *Archives of Biochemistry and Biophysics* 593 (2016), pp. 24–37.

[146] Ayuko Sakane et al. “Conformational plasticity of JRAB/MICAL-L2 provides “law and order” in collective cell migration”. *Molecular biology of the cell* 27.20 (2016), pp. 3095–3108.

[147] Sai Srinivas Panapakkam Giridharan and Steve Caplan. “MICAL-Family Proteins: Complex Regulators of the Actin Cytoskeleton”. *Antioxidants & Redox Signaling* 20.13 (2013), pp. 2059–2073.

[148] Kazuhisa Miyake et al. “Actin cytoskeletal reorganization function of JRAB/MICAL-L2 is fine-tuned by intramolecular interaction between first LIM zinc finger and C-terminal coiled-coil domains”. *Scientific reports* 9.1 (2019), pp. 1–13.

[149] Ayuko Sakane et al. “JRAB/MICAL-L2 undergoes liquid–liquid phase separation to form tubular recycling endosomes”. *Communications biology* 4.1 (2021), pp. 1–16.